3-D Visualization of a Zero-Pressure Gradient Turbulent Boundary Layer

by

Steven Tyler Williams

A thesis submitted to the Graduate Faculty of
Auburn University
in partial fulfillment of the
requirements for the Degree of
Master of Science

Auburn, Alabama
August 9, 2010

Copyright 2010 by Steven Tyler Williams

Approved by

Brian Thurow, Chair, Associate Professor of Aerospace Engineering
Roy Hartfield, Professor of Aerospace Engineering
Andrew Shelton, Assistant Professor of Aerospace Engineering

Abstract

The application of a novel technique for 3-D visualization of a zero-pressure gradient turbulent boundary layer is discussed. Measurements of a 1.65δ x 1.65δ x 1.65δ volume were taken at a flow speed of 96 ft/s, Re_θ ~ 5900, and δ = 1.21 in, in a 2 ft x 2 ft open circuit wind tunnel. Many different mechanisms for flow seeding were explored in order to find the most sufficient technique. Experiments were run to ensure that the boundary layer was not being adversely affected by the flow seeding technique and that a zero-pressure gradient was being maintained. 2-D PIV experiments were also run to give a quantitative comparison to the qualitative data from the 3-D measurement technique. Resulting 3-D measurements illustrated the existence of large-scale structures in the boundary layer, giving a unique look at a flow speed and volume combination previously uncharted in 3-D boundary layer measurements. The quality of the 3-D measurements proved that the flow seeding technique used in these experiments was satisfactory and laid the foundation for future measurements in a variety of flow conditions.

Acknowledgements

I would first like to thank God for blessing me with the opportunity to continue my education at Auburn University in pursuit of a Master's degree. I have absorbed a vast amount of knowledge within my past two years of graduate school and will carry that knowledge with me for the rest of my life. Many thanks go to Dr. Thurow for his offer to work under him as a graduate research assistant. His open-door policy and critique has been extremely helpful throughout this research. I would also like to thank Zach Reid, Blake Melnick, Abhishek Bichal, and Kyle Lynch for their assistance and suggestions during this research. They have been a conduit for many ideas during my time as a graduate student and their help is greatly appreciated.

I would also like to thank my family for their support throughout my academic career. My mother and father have always been very encouraging in my endeavors and their support has been uplifting. I would especially like to thank my wife for her encouragement and support during my pursuit of a Master's degree. She has always been an inspirational part of my work and my life, and has been extremely tolerant of my long nights spent working toward the completion of this research.

Table of Contents

List of Tables

viii

List of Figures

Nomenclature

y – normal distance from wall

$y+$ - dimensionless wall unit

u – velocity vector

u_τ – friction velocity

$u+$ - dimensionless velocity vector

$\bar{u}$ – mean component of velocity

u' – fluctuating component of velocity

ν – kinematic viscosity

κ – Karman's constant

ω – vorticity

ρ – density

Γ – state of the ensemble at a given time

p – pressure

x' –distance from origin in x-direction

δ – boundary layer thickness

θ – momentum thickness

U_∞ - freestream velocity

FOV – field of view

ξ – size of largest dimension of interrogation region (in pixels)

D – displacement

M – magnification

V_o – interrogation volume

s – separation vector

R_C - convolution of the mean intensities of the intensity field

R_F - noise component of the intensity field

R_D - correlation of images of the intensity field

Re_θ – Reynolds number based on momentum thickness

1 INTRODUCTION

1.1 Overview

Turbulence has been the source of great debate within the aerospace community for quite some time. Its inherent three-dimensional, chaotic, and nonlinear nature has in fact proven it to be one of the most challenging problems in physics. To date, the most effective means of both the creation and validation of theoretical assertions has been through the use of flow visualization and observation.

There is a great deal of demand for knowledge of turbulence in many fields of study. The automotive industry could benefit greatly from being able to reduce the effects of turbulence in order to decrease drag and increase fuel efficiency. At the astronomical level, turbulence is the cause of the earth's magnetic field and the production of solar flares from the sun. Even the medical industry could benefit from a better understanding of turbulence, as the arrangement of vents and furniture in rooms play a big role in flow dynamics in the hospital, directly affecting comfort for patients in their rooms or even surgeons during lengthy procedures. It is clear that the ongoing studies on turbulence have a wide variety of potential applications. **This thesis describes the application of a novel 3-D flow visualization technique for the investigation of a turbulent boundary layer.**

Turbulent boundary layers are extremely complex in nature. They are highly erratic and random and they evolve both in space and time. This makes predicting the structure of turbulent boundary layers a challenging task. Many models currently exist to

predict them, such as Large Eddy Simulation (LES), Reynolds-Averaged Navier-Stokes Equations (RANS), and Direct Numerical Simulation (DNS). However, all of these models are limited in some way. For instance, LES is an excellent model for free shear flows at high Reynolds numbers, but is not as fit for modeling turbulent combustion or turbulent boundary layers on a smooth wall.[1] DNS requires much more computational effort than LES or RANS. The averaged solutions that RANS provides are less reliable than the other turbulence models. Add to this the constraint that LES and RANS have due to the famous closure problem of turbulence and the limitations of these predictors become quite evident.

On the experimental side, flow visualization has proven to be a highly efficient technique for both qualitative and quantitative analysis. In this procedure, the flow near the wall is seeded with small particles (or dye if using a water tunnel). A laser (typically pulsed to increase peak power) light sheet illuminates the seeded flow. The particles in the flow scatter the light, and a camera takes images of the plane. The result of a quantitative analysis of these images, such as particle image velocimetry, is a velocity vector map, whereas qualitative analysis is used more as an observational tool. One obvious advantage of flow visualization over numerical models is that flow visualization will give a more accurate representation of a turbulent flow since it is taken in real time. The challenge is resolving the flow in three dimensions. However, using a pulse burst laser in conjunction with a high speed camera triggered to take an image of each pulse as it traverses depthwise into the volume allows the visualization of a volumetric flow field.

Given the lack of knowledge that still exists in the field of turbulence, there are still many questions that have yet to be resolved. For instance, what kinds of effects do

large-scale structures have on a turbulent boundary layer? What does their presence tell us? Do these effects promote or discourage separation? Which of these structures are present most often? Can the physics of these structures be exploited in order to delay the onset of separation? There have been a multitude of studies on flow control attempting to answer these questions. In the past, those interested in 3-D flow visualization were limited to 2-D measurement techniques. It is clear that a more qualitative experimental approach to 3-D turbulent boundary layers could shed some light on these uncertainties.

1.2 History of flow imaging

Until recently, flow visualization was limited to a qualitative analysis of incompressible flow properties. The earliest observations were made by Leonardo da Vinci, in which he made detailed drawings of the structures present in water flow. The first use of flow visualization is attributed to Ludwig Prandtl. In 1904 he designed a water tunnel driven manually by a rotating blade wheel in which models such as cylinders and wings could be mounted for flow analysis, yet still in a qualitative manner. Streak photography was also implemented in the early 20th century for qualitative analysis. In 1984, Adrian introduced a method for quantitative flow analysis in what is known as Particle Image Velocimetry (PIV).[2] It sparked a great deal of interest with researchers interested in turbulent flows due to its ability to measure a wide range of scales in both length and velocity.[3] Today, PIV is used for a wide range of fluid flow problems, and interest in three-dimensional flow fields spawned a technique based on the principles of PIV known as Scanning PIV (SPIV) which has seen significant use since the early 1990s. This was a breakthrough particularly in the field of turbulence which is inherently a

three-dimensional problem and to this day contains theories that are still largely debated. As technology has continued to improve, more visualization techniques have been established, such as tomographic-PIV,[4] planar laser induced fluorescence (PLIF),[5] and qualitative 3-D flow visualization, the technique presented in this thesis.

1.3 Nature of turbulence and boundary layers

Much is still unknown about the nature of turbulent boundary layers. From a classical standpoint, a turbulent boundary layer is made up of four different sections: a viscous sublayer, a buffer layer, a log layer, and an outer layer. The region closest to the wall is called the viscous sublayer. It exists at roughly y+ < 5, where y+ is the wall unit normal to the wall, or

$$y+ = y\left(\frac{u_\tau}{\nu}\right)$$

where y is the normal distance away from the wall, u_r is the friction velocity , and ν is the kinematic viscosity of the fluid. The velocity non-dimensionalized by the friction velocity is typically used in statistical analysis of the boundary layer and is defined by

$$\frac{u}{u_\tau} = u+$$

The viscous sublayer behaves (partially) like a laminar flow due to viscous forces dominating this region of the boundary layer. Because the vorticity in a boundary layer originates from the surface, the viscous sublayer is subjected to bursts of fluid ejected from the wall. The vorticity then either diffuses upward or advects. The buffer layer exists at an approximate region of 5 < y+ < 40 and is a cross between the viscous

sublayer and the log region. The log region applies at y+ > 40 and is a region dominated by inertial forces. It is based on the log-law of the wall, defined as

$$\frac{u}{u_\tau} = \frac{1}{\kappa}\ln(y+) + 5.5$$

The Karman's constant is κ and is approximately 0.4. This equation has been shown to be a strong fit to experimental data and as such is used frequently in the field of turbulence. Within this log region, the distance near the wall is the relevant length scale, and because of this plots of quantities such as Reynolds stresses are typically plotted against wall units for analysis.

Beyond the log region is the outer layer. This is the outer portion of the boundary layer that exhibits a convoluted shape which represents the vorticity that has been advected by large scale structures within the boundary layer. Here, the boundary layer thickness is the relevant length scale. It is highly intermittent, meaning that the instantaneous edge of the boundary layer at any given position fluctuates chaotically in time. Within this region of the flow, the length scales tend to approach the boundary layer thickness. This makes visualizing the structures in the outer layer comparatively easy, and the focus of this thesis will be investigating the outer layer. The characteristics of this outer region are also largely dependent on the freestream pressure gradient as well as the global flow characteristics. For instance, an adverse pressure gradient leads to a decrease in kinetic energy of the flow and hence a decrease in momentum of the fluid. This decrease in momentum has a considerable affect within the inner layer, slowing down the fluid and in some cases reversing the flow. This causes the outer layer to transport kinetic energy to the inner layer. As a result, the dynamics of the flow field are changed substantially compared to a turbulent boundary layer with no pressure gradient.

Recently, turbulent boundary layers have been handled from a statistical point of view. As stated above, the turbulent boundary is traditionally split up into a viscous sublayer, a buffer layer, a log layer, and an outer layer. The advantage of this approach is its universality. This statistical method can generally be applied to any turbulent boundary layer. The drawback to this method is the assumptions made in this viewpoint, particularly in the log layer. The assumption is that turbulence near the wall is independent of the boundary height. This is not actually true. However, the assumption is still safe in practice because the velocity fluctuations near the wall have a negligible contribution to Reynolds stresses, leading to a very small influence on the mean velocity profile near the wall.

Relatively recently an illustration of eddies and large-scale structures has been drawn to describe the process of turbulence. It is understood that instabilities in the mean flow are what bring about eddies. The largest eddies in a turbulent flow are introduced to inertial instabilities which results in a break-up into smaller eddies. The smaller eddies undergo the same process and so on. Each of these progressions results in a transfer of energy to the next scale of eddies. The progression stops when the smallest eddies cannot overcome viscous forces, i.e. viscosity dominates the inertia of the eddies. This process results in what is called an energy cascade.[6] The mechanism for this energy exchange is quantified as Reynolds stress. The Reynolds stress results in a net force that acts on the mean flow. As a result, the mean flow loses energy to turbulence. This transfer of energy causes an increase in stress and the cycle continues down to the smallest eddies.

A strong contribution to Reynolds stress in turbulent boundary layers come from large scale structures known as hairpin vortices. These vortices are usually oriented at 45

degrees to the mean flow but generally align themselves in the direction of the principal strain rate. The stretching of these vortices leads to an increase in kinetic energy and therefore more energy exchanged from the mean flow to turbulence.[7] Closer to the wall (y+<50), however, pairs of streamwise vortex tubes are dominant. These tubes interact with the streamwise vorticity which results in a velocity which is lower than the fluid surrounding them. These structures are known as low-speed streaks, and are on the order of 10^3 wall units long. It is thought that these streaks are eventually ejected from the wall region after interacting with the streamwise vortices, resulting in instability in the fluid. In fact, many researchers in turbulence believe this connection to be one of the primary mechanisms of turbulent energy generation in a boundary layer, even though there are varying ideas on how this energy generation takes place.[8,9] The statistics used to describe the flow field reveals nothing about the structures in the boundary layer that created these statistics. Flow visualization experiments to supplement the statistics of the flow would be extremely helpful since the analysis of a large-scale structure such as a hairpin vortex could ultimately help describe some of the statistical terms (namely Reynolds stresses) that derive from the presence of these structures. Hence it is these structures that command a great deal of attention in turbulent flows

1.3.1   Relation to this Research

Recently, a picture of what is referred to as a hairpin vortex has become the most famous of all the coherent structures in a turbulent boundary layer thanks to flow visualization studies. These hairpin vortices appear in a wide range of Reynolds numbers and generally incline at a 45 degree angle with respect to the flow direction, arching up

from the surface. It is thought that these vortices make significant contributions to Reynolds stresses and therefore apply to both the inner and outer structure of the boundary layer. However, this picture has been under dispute for quite some time as the appearance of these structures is a mushroom-like feature when visualized in a single plane via flow illumination. **With research into the flow field through multiple planes (3-D flow visualization), a clearer picture of the large scale structures in a turbulent boundary layer is possible. Hence, the motivation of this research is to document the application of a novel 3-D flow visualization technique on a turbulent boundary layer at a freestream velocity of 96 ft/s and Re$_\theta$ ~ 5900.**

1.4 Recent attempts at flow visualization

Flow visualization has seen many different techniques introduced throughout the history of aerodynamics, from smoke wires[10] to dye injection. More recently, fog machines have been used by many researchers as a way to supply a significant amount of particles for non-invasive flow seeding. Usually, this type of flow seeding is used to visualize the flow over a large viewing area. In the case of boundary layers, however, the viewing area is much smaller, and visualizing the flow seeding over an area so small can prove to be quite challenging, especially when the goal is to identify the large-scale structures in a turbulent flow. The use of a high-energy laser remedies this problem due to the large energy output.

A 3-D flow visualization technique similar to the technique presented in this thesis is called tomographic-PIV. It is a quantitative measurement technique that uses four cameras to visualize particle within a flow field, thereby giving 3-D velocity data.

With high frame rate cameras used in conjunction with high repetition rate lasers, time-resolution is also possible. In fact, current tomo-PIV studies have produced 3-D results of vortical structures. However, tomo-PIV comes with high computational costs which make the time-resolved measurements impractical at times.[11] Other problems include errors associated with the image reconstruction algorithms that can sometimes be significant enough to compromise the quality of the data. 3-D flow visualization, on the other hand, does not require long computational time but is currently limited in time resolution. One big advantage of 3-D flow visualization is the much larger volume it can capture. This is key when visualizing a volume in which coherent structures larger than one boundary layer thickness in size might exist. Tomo-PIV would have a hard time capturing these structures in those kinds of flows which is why tomo-PIV experiments are classically limited to mm x mm x mm volumes. Tomo-PIV experimental setups are also much more complex compared to the visualization technique used in this thesis, requiring multiple cameras and clever optical arrangements for best results.

Previous experiments done by Delo and Smits are similar to the work presented in this thesis.[12] They performed 1600 volumetric visualizations (composed of 20 uniformly-separated streamwise-normal images of scalar intensity) on a turbulent boundary layer on a flat plate in a water tunnel at a freestream velocity of 229 mm/s, Re_θ of 701, and δ of 26.9 mm. These visualizations were time resolved, with 40 ms elapsing between each volumetric measurement. Dye was seeded into the flow field by two slits cut into the flat plate; one slit was closer to the leading edge to seed the entire boundary layer while the other slit was further downstream to provide more seeding intensity near the wall. Turbulence was created using a trip wire placed immediately before the first dye slot. A 5

Watt CW Argon Ion laser was used to illuminate the flow, and the 3.53δ x 1.49δ x 3.34δ volume (in x-y-z coordinates, respectively) was scanned using a rotating drum with multiple adjustable mirror mounts. The result of these experiments was a series of stereoscopic images viewable with anaglyph glasses. The images showed large-scale spanwise organization of structures inclined within a range of ±50 degrees with respect to freestream. On average the structures had a spacing of about 1δ, with large variations from case to case. The images also revealed the relationship between near-wall streaks and the large structures in the outer layer. It was seen that one near-wall streak could be responsible for the ejection of multiple fluid packets.

1.5 Uniqueness of this Research

Because previous studies have closely investigated the presence of structures in a turbulent boundary layer, it is important to distinguish this research from preceding experiments. Perhaps the most notable difference in the technique used in this thesis is the speed of the flow field it can resolve. Experiments done by Delo and Smits and Adrian[13] investigated flow fields with a freestream velocity on the order of hundreds of millimeters per second. The experiments performed for this thesis examined the outer layer of a turbulent boundary layer with a freestream velocity on the order of tens of meters per second. This could potentially lead to some new discoveries in the physics of these turbulent boundary layers, such as the connection between faster flow fields and the properties of the large-scale motions and the similarities and differences of these structures at different Reynolds numbers. Further advancements in these experiments could lead to examination of turbulent boundary layers in an adverse pressure gradient,

the effect of flow control mechanisms on the physics of these boundary layers, and even

an investigation into boundary layers in the compressible flow regime.

2   FLOW VISUALIZATION

2.1 Overview

Two flow visualization techniques were used for this research: 2-D particle image velocimetry (PIV) and qualitative 3-D flow visualization. The main focus of this research is on 3-D flow visualization, but PIV measurements are necessary to supplement the qualitative data that comes from the 3-D visualization.

Both flow visualization techniques will be discussed in depth in this section. Characteristics of the techniques as well as the considerations taken in the application of these techniques are presented. Difficulties in implementing a sufficient boundary layer seeding mechanism for the 3-D measurements are also discussed. For reference, a picture and diagram of the facility is shown in Figure 1, with more details of the experimental facility to be discussed later. Pictured in Figure 1 is a 2 ft x 2 ft test section of an open-circuit wind tunnel. A flat plate model was placed in the test section to be used as a platform for studying a zero-pressure gradient turbulent boundary layer. The boundary layer along the flat plate was seeded with particles from a smoke machine. A mirror rig was set up at the top of the test section to direct a laser sheet into the seeded volume of the boundary layer.
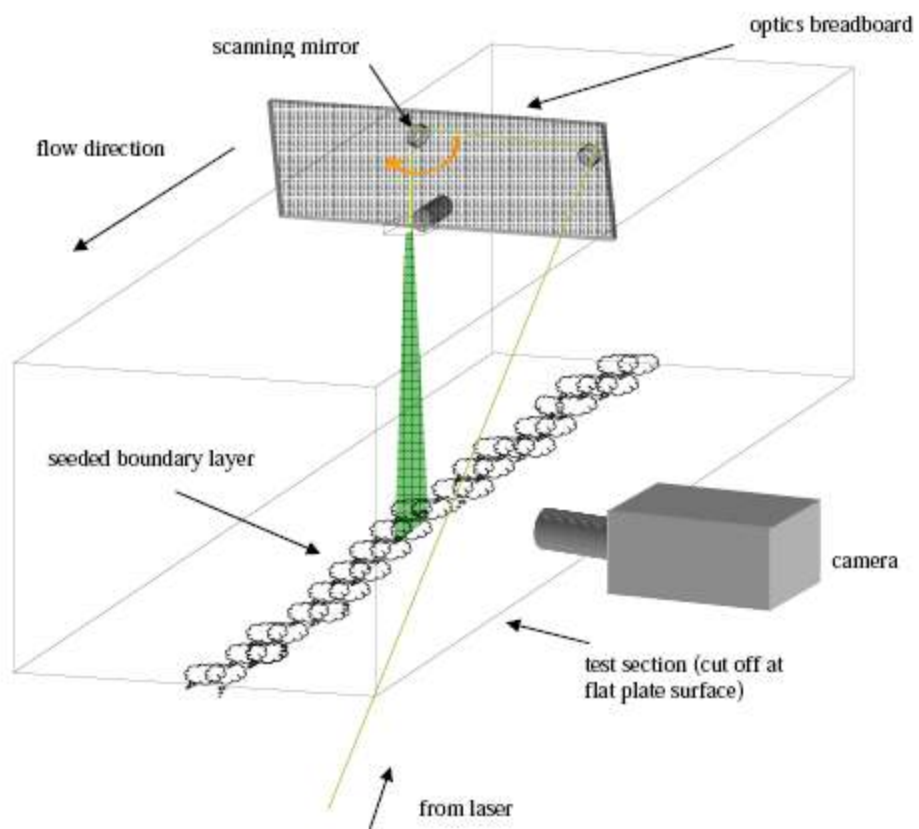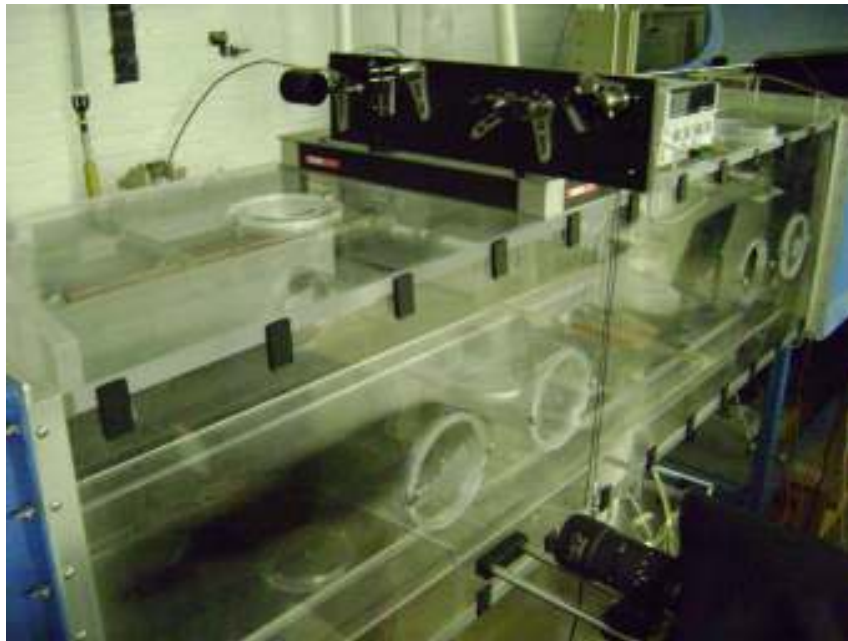
Figure 1: Picture and diagram of the flow visualization facility.

2.2 Particle Image Velocimetry

Particle Image Velocimetry (PIV) is an optical fluid measurement technique used for quantifying the velocity of particles in a seeded flow field. The fluid is seeded with tracer particles and illuminated with a double-pulsed light source. A camera is synchronized to record an image of the flow field at the two light pulses, resulting in an image pair of which velocity data of the flow field can be derived using a variety of algorithms and correlation techniques.

For the PIV experiments in this thesis, the entire flow field is seeded with particles from a smoke machine. The smoke machine used in the PIV experiments is a ViCount Compact 1300 oil-based smoke generator that produces particles 0.2-0.3 microns in size. The mass flow rate of the particles is controlled by increasing the pressure from the pressure source required to operate the machine.

2.2.1   Characteristics

PIV has many advantageous characteristics that make it a widely used tool in modern fluid flow measurements. However, with these advantages also come certain considerations and trade-offs. The key to an effective PIV experiment is finding the best compromise between these trade-offs to ensure the most accurate measurements possible. A general list of the characteristics of PIV is given in this section,[14] with considerations given in section 2.2.3.

•*Nearly Non-Intrusive*: PIV uses tracer particles seeded in the flow in conjunction with a laser and camera to quantify velocity. This has an obvious advantage over measurements with pitot probes or hot wires because the measurements taken with PIV do not perturb

the flow. Granted, even the tracer particles have some measurable effect on the flow, but compared to the other measurements mentioned above, this effect is negligible.

•*Planar Technique*: PIV is a flow measurement technique that extracts velocity information based on images of large parts of a flow field. This makes PIV perfect for unsteady flows that require high spatial resolution and instantaneous imaging.

•*Nearly Instantaneous Flow Measurement*: Today's optical technology allows PIV measurements to be nearly instantaneous flow measurements. As cameras approach framerates of 10 million frames per second and high-repetition rate pulse burst lasers continue to be improved, this characteristic of PIV will only improve with time.

2.2.2   Application to Research

The goal of using PIV techniques in this research is to to verify that the boundary layer in the experiment closely resembles the classical description. Namely, it is known that large scale structures exist in the outer portion of the boundary layer, and that these structures perhaps evolve from smaller structures in the inner portions of the boundary layer that exist due to the presence of vorticity near the wall. Direct numerical simulations can only typically predict these structures at low Reynolds numbers. PIV measurements, on the other hand, can be used to reveal many physical characteristics of the boundary layer at higher Reynolds numbers, such as the statistics of the boundary layer (Reynolds stresses, friction velocity, etc) and the momentum layers that hold these large-scale structures. This is something that a more qualitative approach, such as the 3-D flow visualization technique discussed in this thesis, cannot resolve. Most importantly, averaging all of the images acquired by the PIV experiments will give us an average

boundary layer thickness, which will be used to ensure that the flow seeding for the 3-D flow visualization experiments is accurately tracing the boundary layer. It will also provide a rough measure of the pulse scanning distance for the 3-D flow visualization measurements so that, on average, each 3-D measurement captures the entire boundary layer.

The data acquired from instantaneous PIV measurements should look similar to the data shown in Figures 2 and 3, which is data taken from Adrian (2000) where experiments were performed for three Reynolds numbers within the range $930 < Re_\theta < 6845$. Figure 2 shows a plot of velocity vectors for a boundary layer at $Re_\theta = 2370$ with 80% of freestream velocity subtracted, and Figure 3 shows layers of constant momentum. Both plots are in wall units, and the heads of the structures are circled with black lines going through the center of each head and tracing out the momentum layers. The heads appear at the edge of their respective momentum layer, and it was shown that there is indeed a direct relationship between these large-scale structures and the uniform momentum zones. If the PIV experiments performed for this thesis have close relation to the results from Adrian (2000), it would provide a strong validation of the experimental setup described here, as it would give confirmation that the flow field closely resembles previous studies on a turbulent boundary layer.
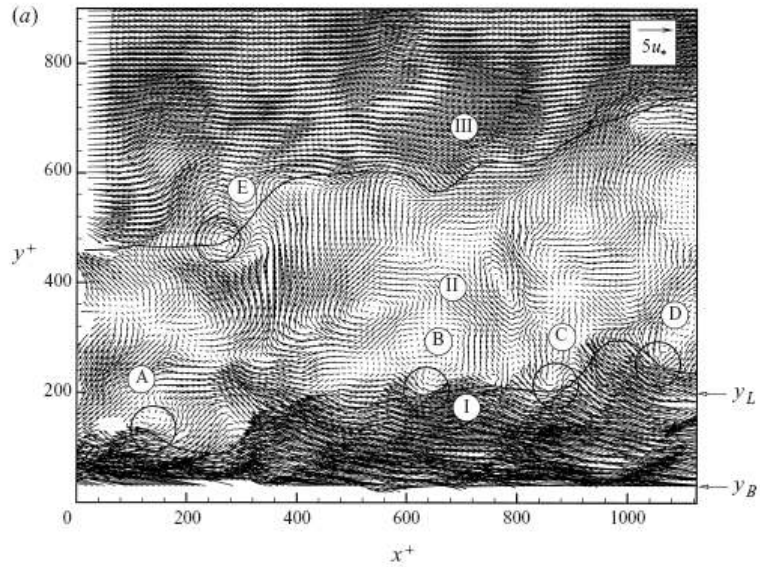
Figure 2: Plot of velocity vectors from data acquired by Adrian (2000) for a boundary layer at $Re_\theta=2370$.
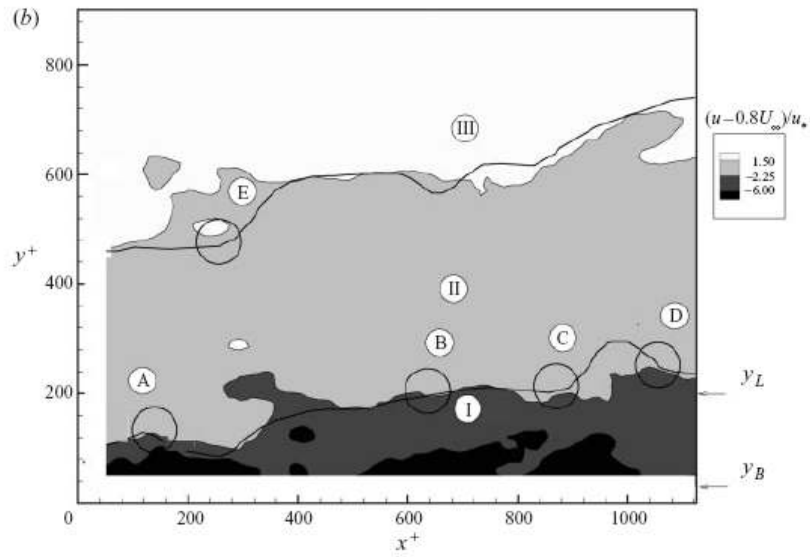
Figure 3: Plot of momentum layers from data acquired by Adrian (2000) for a boundary layer at $Re_\theta=2370$.

2.2.3   Considerations for PIV Experiments

During the PIV experimentation and the analysis of the data, some considerations

were made. Those considerations are listed in this section.

2.2.3.1 Field of View

In order to accurately measure the particle displacement depicted in the images, the field of view of the camera must be measured. This is done quite simply by placing a dot card in the field of view. Each dot is spaced equally from the other dots so that a value of pixels per inch can be calculated. This information is also used when doing the calculations for a proper time interval between each pulse and image as discussed in the next section.

2.2.3.2 Time Interval Calculation

Calculation of the time interval is based on three fixed values: the desired interrogation region, the maximum speed of the flow field, and the field of view. From *Particle Image Velocimetry: a Practical Guide* (Ref. 14),

$$\frac{U_\infty * FOV}{\xi} = \frac{1}{\Delta t}$$

where U_∞ is the freestream velocity, FOV is the field of view in pixels per length, and ξ is the desired size of the largest dimension of the interrogation region in pixels. The result, Δt, is the time step that should not be exceeded in order to use the specified interrogation region. Otherwise, the results of the flow field interrogation will be inaccurate.

2.2.3.3 Particle Size and Distribution

It is imperative that the tracer particles used follow the flow faithfully. Small particles are the most desirable for this and lead to low velocity lag. Larger particles have a larger scattered light intensity but lead to a higher velocity lag. The particles used in the

PIV experiments are 0.2-0.3 microns in size, which is small enough to ensure accurate flow tracing due to the low settling velocity of the particle reported by the manufacturer (8 mm/hr). The lower light scattering due to the small size of these particles is not an issue due to the light source used for the measurements which is described in section 4.2.4.

It is also essential that the tracer particles are seeded evenly in the flow for the most accurate measurement since a more even distribution improves image density. This requires experimentation with flow seeding techniques in order to find a technique that is sufficient for this experiment. Ultimately, it was decided that seeding the entire room with particles and allowing the wind tunnel to constantly recirculate these particles was the best technique. Care had to be taken to ensure that enough particles were distributed throughout the room, but not so many that the particle density would be too high as to cause the correlated data in the PIV software to be too noisy to achieve accurate data.

2.3 3-D Flow Visualization

The 3-D flow visualization technique used in this research is a qualitative means of analyzing the 3-D features in the boundary layer. This technique requires light sheets produced in multiple planes at extremely small time intervals (small enough to consider the data set a nearly instantaneous representation of the flow field) in coordination with a high-speed camera to get a volumetric scan of the flow field.[15] It also requires a number of post-processing techniques to piece the resulting image sequences from each plane together into one 3-D data set.

For 3-D flow visualization, the goal is to only seed the boundary layer as opposed to the entire flow field as done in PIV. A method for achieving this is described in section 4.4.2. The 3-D flow visualization technique works by utilizing a pulse burst laser in conjunction with a high-speed camera and scanning mirror in order to capture a series of 2-D planar images of the seeded boundary layer illuminated by the laser. Those images are combined to make one 3-D image.

2.3.1   Characteristics and General Restrictions

The 3-D flow visualization technique presented here has similar characteristics to the ones described in the previous section on PIV. It is a nearly non-intrusive flow measurement technique, with the tracer particles having a negligible effect on the flow. It is also nearly instantaneous and can therefore accurately capture the 3-D characteristics of the large scale structures in the flow field. High particle density is desired for this technique to ensure that the entire boundary layer is sufficiently seeded so that variations in intensities in the resulting images are more likely to be a reflection of the physics of the flow field and not due to insufficient seeding. Even so, it should be noted that intensity variations between seeded and unseeded fluid are the primary focus for this flow visualization technique, whereas variations in intensity closer to the wall are typically disregarded.

Some restrictions of this 3-D flow visualization technique are shared with PIV, such as particle distribution and pulse duration. Beyond these, the main restriction in this technique is that it is qualitative. In this regard, we can only comment on the visible characteristics of the flow field, such as the size and shape of the observed structures in

the boundary layer. Furthermore, this technique tends to only reveal the organized structures in the outer layer, so characteristics in the inner layer are often not observable.

2.3.2 Application to Research

Because the relatively recent illustration of large-scale structures in a turbulent boundary layer has been a topic of great dispute, heavy research is required to give a clearer picture of the characteristics of these structures. For this thesis, a zero-pressure gradient turbulent boundary layer is studied to solidify the measurement technique for this flow field by laying a foundation for effective and accurate measurements. The measurements will also provide some clarification on the previously-mentioned illustration. Beyond this research, this technique will provide a means by which to study the characteristics of these structures under a plethora of conditions, such as transition to turbulence, the consequences of adverse pressure gradients, and even the effectiveness of flow control mechanisms to reduce the influence of these structures on the boundary layer.

2.3.2.1 Camera

The camera plays a pivotal role in data acquisition for this research. It is imperative that the camera provide high-quality images and be capable of extremely high frame rates for nearly-instantaneous flow imaging. The DRS Hadland Ultra68 camera fulfills both of these requirements with its capability to achieve frame rates as high as 500,000 frames per second with exposure times as low as 10 ns. This camera utilizes a quadrant design for image acquisition by dividing incoming light with a four-way beam

splitter onto a four-quadrant image intensifier, with each quadrant acting independently from the others. Behind the intensifier is the CCD which records the images from each quadrant. The CCD for this camera is masked with an opaque film to block light from 16 out of every 17 pixels. When light is absorbed by the unblocked pixel, one of the other 16 pixels stores the resulting charge. As a result, 17 images can be stored on the CCD at once. The four-quadrant design of the camera means that a total of 68 images can be stored at a resolution of 220 x 220 pixels.

2.3.2.2 Field of view

In order to accurately measure the characteristics of the large-scale features depicted in the images, the field of view of the camera must be measured based on resolution. This is done quite simply by placing a dot card in the field of view. Each dot is spaced equally from the other dots so that a value of pixels per inch can be calculated. In order to correct for field of view changes from the first pulse to the last pulse, a second dot card image is taken at the rearmost image plane. Corrections for this change in field of view are described in the image processing section.

2.3.2.3 Depth of field

It is imperative that the distance from the front image plane to the rearmost image plane be measured so that the image volume can be properly resampled during the post-processing phase. The depth of field is recorded by measuring the distance between the first and last pulse in the pulse burst train as deflected by the scanning mirror. A 2-inch

depth of field was used for these experiments in order to achieve a cubic volume of 2 in x 2 in x 2 in

2.3.2.4 Flow Seeding Mechanism

The most difficult part of this research was the implementation of a sufficient flow seeding mechanism for 3-D flow visualization. Testing of various mechanisms took up the vast majority of research time. This is because each mechanism had to be tested not only for the quality of the flow seeding, but also for the potentially negative effects it might have on the flow field.

The first technique we attempted involved placing a flow seeding nozzle at the entrance of the wind tunnel and using the surface of the wind tunnel as the flat plate. The nozzle was designed with a converging section to make a thin sheet of smoke particles that would follow the boundary layer. It also diverged in the spanwise direction to widen the potential scanning width for 3-D measurements. A model of the nozzle is shown in Figure 4. The problem with this design was that the seeding would sometimes appear outside the boundary layer. This made it difficult at times to discern what could have either been a large scale structure that was ejected from the outer layer or what simply could have been an artifact of the flow seeding technique.
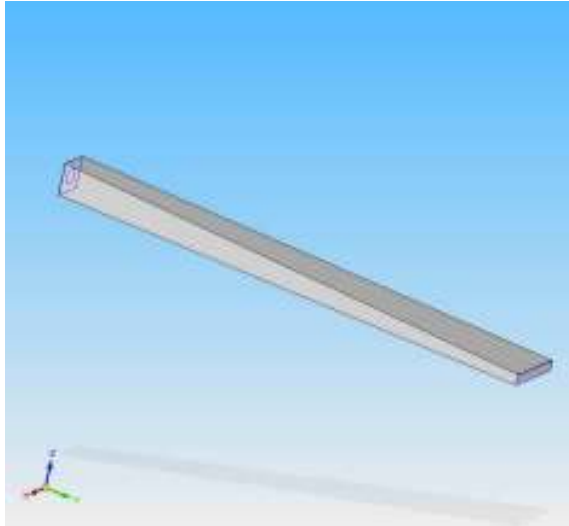
Figure 4: Model for the nozzle used in the first flow seeding attempt.

The second seeding technique attempted was the use of a slowly diverging nozzle, with a picture of this nozzle provided in Figure 5. It was attached to the bottom of the leading edge of a flat plate model placed in the test section and fed smoke particles from a pipe attached to the vacuum end of the nozzle. This provided much more efficient seeding that never appeared to go outside the boundary layer. However, pitot probe and PIV testing showed that the nozzle was having a substantial effect on the physics of the boundary layer. Namely, comparing the velocity profile of the normal case to the velocity profile with the nozzle attached to the flat plate showed that the nozzle was creating a much larger boundary layer thickness (about twice as large as normal). A hypothesis as to why this is the case is that the nozzle was exacerbating the amount of flow reversal at the leading edge, causing the boundary layer to have a much larger initial thickness than would normally be the case.

Figure 5: Picture of the nozzle used for the second flow seeding attempt.

After extensive review of literature from previous flow seeding methods, it was determined that the best course of action was to cut a 0.125 inch slit through the flat plate near the leading edge. Previous work done by Smits and Delo (1997) utilized a pair of slits for dye injection in a water tunnel: one near the leading edge for illumination of the entire boundary layer, and one close to the field of interest to distinguish the inner layer. Shortly before the leading edge slit, a trip wire was used to create turbulence in the boundary layer. For this thesis, however, one slit was used since we are mainly concerned with the outer layer features. Furthermore, a piece of 50-grit sandpaper was placed after the slit so that the induced turbulence from the sandpaper would dominate any effects the slit might have on the boundary layer. Comparing pitot probe and PIV measurements of the case with only sandpaper to the case with the slit and sandpaper confirmed the validity of this setup, showing that the slit had no measureable effect on the flow field.

2.4 Pulse Burst Laser System

The key to a nearly non-invasive flow visualization technique is the effective use of a lighting system. For the purposes of this research a laser system is used. It is essential that the laser has the capability to supply a sufficient amount of energy to illuminate the flow. In conjunction with the first requirement, the laser must also provide that energy in a short duration - on the order of 20 ns for the application presented in this thesis – in order to maintain a nearly instantaneous 3-D image and low duty cycles. Finally, a method to synchronize the laser pulses with the camera must be implemented. The technique used in this research utilizes all of these requirements with the capability of sampling a flow volume at near-MHz rates.

The laser used in the Auburn University Advanced Laser Diagnostics Laboratory is a third-generation pulse burst laser.[16] It is capable of repetition rates in excess of 1 MHz. For the purposes of this research, a 68-pulse train of 20 ns duration pulses (measured at full-width, half-maximum) was used with 2 μs between each pulse (500 kHz), resulting in a total pulse train duration of 136 μs and pulse energies on the order of 10 mJ/pulse. These specifications are adequate for both the mJ/pulse energies required to sufficiently illuminate the flow and the fast sampling of the volume for a nearly-instantaneous measurement.

2.4.1   Laser components

There are a number of components that make up the pulse burst laser system. A description of the devices required to fulfill these requirements is given below. It should be noted that the information presented in this section is based on previous works from

26

the Advanced Laser Diagnostics Laboratory,[17] but is provided here due to its relevance in the boundary layer imaging techniques presented in this thesis.

A 100 mW continuous-wave neodymium-doped yttrium aluminum garnet (Nd:YAG) laser provides the initial laser power at a wavelength of 1064 nm and a beam diameter of 0.45 mm. The energy from the laser is passed through a Faraday isolator to prevent reflected light from entering the master oscillator. The light is then focused into an acousto-optic modulator (AOM), a device that applies a sound wave with a given frequency which interacts with the laser beam and applies a Doppler shift to the laser beam similar to the frequency of the sound wave. For this research, the AOM is used to create a 68-pulse train of 20 ns pulses that occur in a time of 136 μs (500 kHz).The pulses are then passed through a series of solid-state laser amplifiers. After amplification, pulse energies are increased by a factor of about 10^7. It is important that the amplification process be set up efficiently such that these amplifiers can provide sufficiently high energy/pulse levels. The pulses must then be frequency doubled, also known as second harmonic generation (SHG). Nonlinear optical crystals are used to achieve a 532 nm wavelength light. The crystal also corrects for phase differences between the 532 nm light created at each point in the crystal because of the different refractive indices along the three axes of the crystal. After the light is converted, it is passed to a scanning mirror and a cylindrical lens for volumetric illumination of the flow field. A GSI Lumonics VF500 galvanometric scanning mirror is used and has a tested angular velocity of 100,000 deg/s.

A critical component of the pulse burst laser system is the method for synchronization. The camera must fire the moment one pulse from the laser has illuminated the flow field. Furthermore, a signal must somehow be given to the AOM to

create the pulses. Another signal must then be given to the scanning mirror to trigger its rotation once the pulse train begins. The settings for all of these components must also have the capability to be defined by the user, i.e. scan rate for the mirror, exposure time for the camera, pulse duration for the AOM, etc.

The initial command to trigger all components is provided by a master trigger on the computer. This command is sent via software called Labview and inputted via a National Instruments NI-6602 Counter-Timer card. After a slight delay that can be changed by the user in Labview, a delay trigger is activated, which tells the AOM to create the pulse burst train. Varying this delay tunes the activation of the pulse train in relation to the flashlamps firing. With correct tuning, this results in nearly-constant energies in each pulse due to constant amplification and depletion rates within the amplifier crystals.

The master trigger mentioned above also sends a signal to a signal generator card which outputs a step signal to the scanning mirror. The Labview program calculates a signal frequency to send to the scanning mirror such that one deflection is generated per pulse. This calculation is based on the pulsewidth of the trigger from the power supply. The signal sent is longer than the calculated signal frequency to ensure that the scanning mirror is allowed ample time to return to its resting state and also provides consistency between pulses. The amplitude of the step signal controls the deflection angle of each pulse, and equal deflection of each pulse is provided by tuning the starting phase of the output signal to activate during an approximately linear portion of the mirror's deflection.

Additionally, the master trigger sends a signal to the camera. The camera used in these experiments has an internal camera delay of 85 ns, so this value is subtracted from

the delay signal from the NI-6602 card in order to synchronize it with the other components. Exposure time is controlled using the external monitor feature of the camera. The signal provided by this feature is sent to an oscilloscope and tuned alongside a signal of each laser pulse provided using a photodiode in order to position the camera exposures with each pulse generation.

3   IMAGE PROCESSING

3.1 Overview

The images from the Ultra 68 camera require various enhancements and conversions in order to properly discern the boundary layer data. Through the clever use of software to convert the images to a different format, apply different image filtering techniques, and employ corrections due to system imperfections, the quality of the original images can be enhanced to get a much clearer view of the data. This section presents a detailed description the post-processing techniques utilized for this research, as well as some examples of data before and after certain enhancements are implemented. An example code for these techniques is provided in Appendix C.

3.2 Software

Two programs are used to create the flow visualization images presented in this thesis. Both are described below.

3.2.1   MATLAB

MATLAB (short for matrix laboratory) is a numeric computing language developed for easy matrix manipulation. The facet of MATLAB we are most interested here is its ability to process images via graphics functions. MATLAB can read many image file extensions including the TIFF files outputted by the Ultra 68 camera software. MATLAB reads each pixel in the file as some intensity value and saves it as a matrix so

that the data can be edited and transformed any way the user sees fit. MATLAB has many predefined functions for processes such as filtering and resizing. For more information on MATLAB, visit www.mathworks.com.

3.2.2   Tecplot 360

Tecplot 360 is a 3-D post-processing tool used for numerical simulation and flow visualization. Though it was designed for processing CFD data, it provides many functions useful for our research, including settings for image intensity plots, axis aspect ratios, number of slices to display, and isosurface renderings. The resulting 3-D data from MATLAB is converted to a Tecplot-compatible format so that it can render the 3-D image in terms of the intensity values stored at each location. From there, the 3-D data can be split into separate planar slices, an isosurface can be plotted, an image threshold can be set, axes can be drawn, etc. More information about Tecplot 360 can be found at www.tecplot.com.

3.3 Corrections

The original images have some imperfections due to the presence of noise, the spatial intensity profile of the laser pulse burst train, magnification errors, and other various considerations. To improve this data to highlight the most relevant features, seven steps are taken to enhance image quality in order to get the best representation of the imaging field. These steps were originally provided by Kyle Lynch from the Auburn University Advanced Laser Diagnostics Laboratory and were modified by the author for use for this specific flow field. An additional enhancement involves edge detection which

is optional and generally applied when we are interested in emphasizing the border of the boundary layer. The steps for these corrections are detailed below.

3.3.1   Dark image subtraction

Even though measures are taken to keep ambient light out of the region of interest, some ambient light will inevitably be present in the images. This introduces noise into the images that has to be accounted for. To solve this problem, a sequence of dark images is taken with the flashlamps from the amplifiers firing but with the laser aperture closed. This dark image sequence is then subtracted from each 3-D image reconstruction.

3.3.2   Ghosting correction

The unique quadrant design of the camera described in the flow visualization section causes some complications in the imaging process.[18] Specifically, the phosphorescent screen utilized by the intensifier on the camera have a slower decay time than the frame rates required for this research. The result is that information from a previous frame shows up in the next image respective to its quadrant, e.g. residual intensity from frame 1 shows up in frame 5. This is a phenomenon known as ghosting, and a couple of different steps can be used to alleviate this problem. A low-pass filter can smooth the ghost images to an acceptable quality. A more meticulous correction that is practiced in this thesis involves recording a set of images from a single, long-duration pulse from the laser and analyzing the resulting intensity profiles across all images in

order to come up with a set of correction coefficients. These coefficients are then loaded into a matrix to be applied to the flow images.

3.3.3 Light sheet intensity normalization

Because of the nearly-Gaussian profile of the laser pulse burst train, values in the middle of the image will have higher intensity than values on the left and right of the image. Furthermore, small spots on the scanning mirror or imperfections on the wind tunnel test section surface could cause localized drops in laser sheet intensity since the light sheet is propagating from top to bottom. Uncorrected, this phenomenon drastically reduces the amount of usable information in the image. In order to get rid of this misleading intensity, a sheet intensity profile is calculated by taking the bottom 20 rows of an individual image and averaging the intensity value of the profile on a column-by-column basis, creating a normalization factor for each column. Each column is then divided by its respective normalization factor to make the light sheet intensity throughout the entire image appear more uniform The entire process is applied under the assumption of constant particle seeding over the bottom 20 rows of the image. This is because it is expected that intensity near the wall should be approximately uniform due to the flow seeding technique used.

3.3.4 Spatial correction

As the laser sheet moves away from the camera (depthwise in the flow field), the field of view increases. This causes discrepancies in magnification between each image. To correct this issue, an image of a dot card is taken in both the front- and rear-most

image plane. The dot card is made of a square matrix of equally-spaced dots and placed on a traversing apparatus to ensure it does not translate side-to-side as the dot card traverses from the front to the rear image plane. The MATLAB program then uses a center-of-mass iteration scheme to linearly interpolate the location of each dot, with the number of dots in the x and y direction predefined by the user in the code. Once the iteration is complete, a guess for dot locations is stored for each of the intermediate images and applied to them using an image transformation function, serving to map each of these images into one common grid for constant resolution.

3.3.5   Filtering

Two different filtering techniques were applied to each image in order to enhance quality. These two filtering techniques are called median filtering and smoothing. The 2-D median filtering algorithm applied in MATLAB (*medfilt2*) is a neighborhood operation, meaning that the value of any one pixel is a function of a predefined number of pixels surrounding it. The algorithm is non-linear in nature because it **does not** imply that the value of the new pixel is a linear combination of the old pixels surrounding it. In the case of pixels at the edge of an image, values for pixels outside of the image area can be defined by either using zero padding or border replication. Zero padding is when values for off-edge pixels are set to zero. For border replication, values for off-edge pixels are determined by replicating the value from their respective nearest border pixel. The default operation for MATLAB's median filter uses zero padding, and although other padding options can be implemented, zero padding would be sufficient for this work since preservation at the image borders is not a necessity.

On the other hand, MATLAB has a built-in 3-D smoothing function (*smooth3d*). This function smoothes the data by taking the mean value of a predefined number of surrounding pixels (3 x 3 by default in MATLAB) and replaces the pixel with that mean value. MATLAB gives functions for smoothing by Gaussian or box filtering and then determines the convolution kernel to apply to the 3-D matrix.

It should be noted that a smoothing filter replaces values using the mean value of the surrounding pixels in the interrogation region. A median filter replaces values using the median value of the surrounding pixels. Therefore, applying a median filter gives a stronger average than the mean because one spurious pixel intensity value will not affect the median value as significantly. This helps preserve stronger edges compared to a smoothing filter. On the other hand, the 3-D smoothing function in MATLAB has obvious advantages over the median filter in that the smoothing filter acts over the entire 3-D matrix and not just each individual 2-D slice. Since the current focus of this 3-D flow visualization technique is the larger structures in the outer layer, stronger edge preservation is not a concern. This makes choosing the 3-D smoothing filter over the 2-D median filter justifiable.

3.3.6   Image thresholding

Nonzero intensity values are stored even in a figure of a dark image due to factors such as ambient light. This can prove to be bothersome when uploading sequences in Tecplot for flow visualization, as blotches of erroneous data can show up in planar images and isosurface renderings. A correction for this is to set a reasonable minimum

intensity value and have MATLAB set all values below this threshold to zero. The resulting image is then saved over the original one.

3.3.7   Resampling

In order to make the resulting sequences reflect the actual volume of the field of view measured, the original 220 x 220 x 68 sequences are converted to a 220 x 220 x 220 volume, with the third dimension calculated by converting the width of the 3-D scan from inches to pixels. There is a function predefined in MATLAB to do this called **imresize**. It uses nearest-neighbor interpolation by default. Nearest-neighbor is very fast but introduces aliasing effects at edges. However, it does preserve original grey level values, whereas bilinear interpolation and cubic convolution do not. Bilinear interpolation is used in this research. It considers a 2x2 neighborhood of surrounding pixels and takes a weighted average of the four pixels to get an interpolation value. The images resulting from bilinear interpolation are therefore smoother than images derived from nearest-neighbor interpolation, which is the motivation for choosing the bilinear approach. The lack of grey level value preservation in the image is not an issue here since the entire intensity profile is reduced by a certain amount, and not just certain portions of the image.

3.3.8   Edge detection

In some analyses we only want to look at the thickness of the boundary layer. To accomplish this, a Sobel filter is applied after all other corrections to reveal a boundary layer edge. A Sobel filter works by calculating image intensity gradients at each pixel of

an image. To do this, values in a 3x3 region around the pixel are used for the calculation, and only integer values are assigned to the intensity values surrounding the pixel in question. This causes a reduction in accuracy of the resulting image gradient compared to other edge detection algorithms, but for this research the Sobel filter is sufficient since we are mainly interested in the locations of maximum gradients. The results of the Sobel filter can be saved in a separate file so that this file can be uploaded in the same layout as the corresponding boundary layer image, showing both the main image and an outline of the boundary layer surface.

3.4 Order of Operations

Figure 6 presents a flow chart of the various image enhancement techniques utilized in the 3-D data presented in this thesis. Some of the image enhancement techniques described above, specifically the ghosting and spatial corrections, were not used in the final processing of the data. The motivation for leaving out spatial corrections was that the depth of field was small enough (2 inches) that the implementation of these corrections was negligible. Ghosting issues from the camera only appeared in the 67th frame of some of the sequences, allowing ghosting corrections on an image-by-image basis to be left out for speed purposes. A proper procedure for removing the ghosting signal is currently under development, so this technique was not implemented in this work.
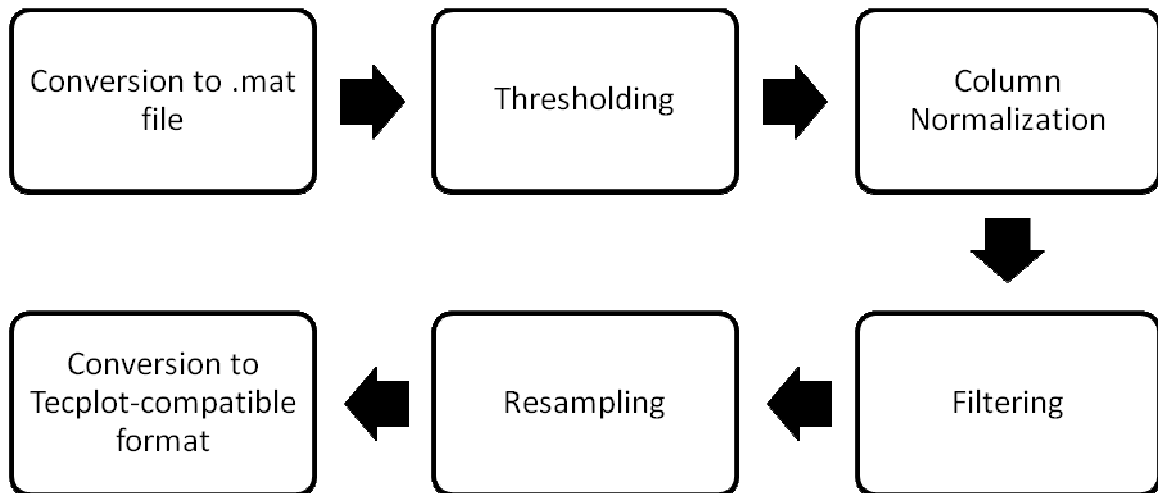
Figure 6: Image post-processing flow chart

3.5 Post-processing Examples

An example of the post-processing procedure from one particular image from the 3-D experiments is presented here in order to illustrate the results of applying these techniques. The images are presented in an RGB color map in order to more easily depict the changes over each correction. They are also presented in the same order that is given in the flow chart in Figure 6.

Figure 7 shows the original image before any corrections are made. The inconsistencies in the laser sheet intensity are apparent, especially in portions where the intensity drastically drops. This was due to damaged portions of the scanning mirror reducing the amount of light reflected in certain areas.
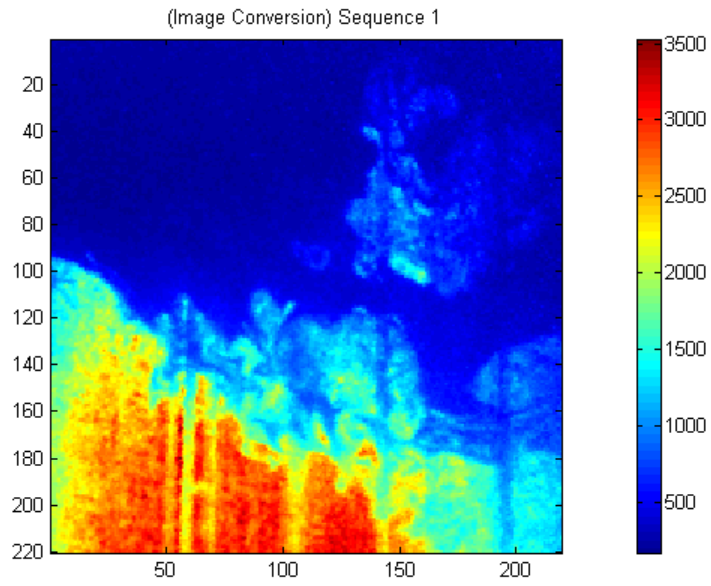
Figure 7: Image before corrections are applied.
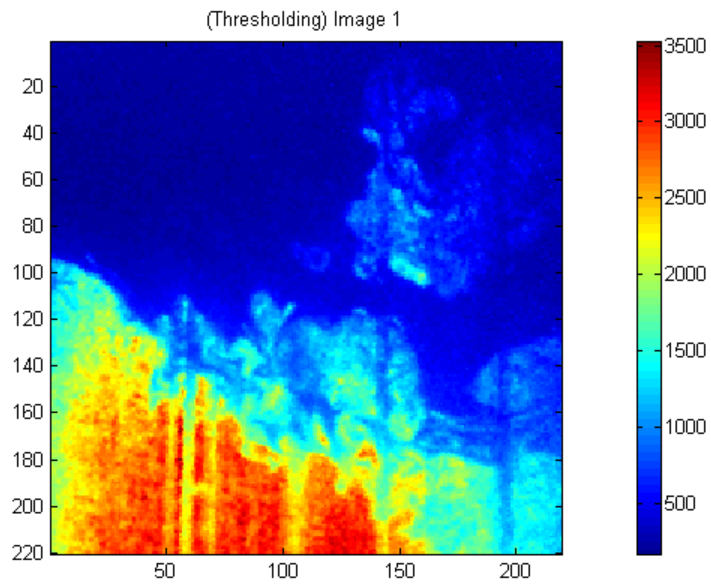
Figure 8: Image after thresholding. Values with intensity less than 100 were set to 0.
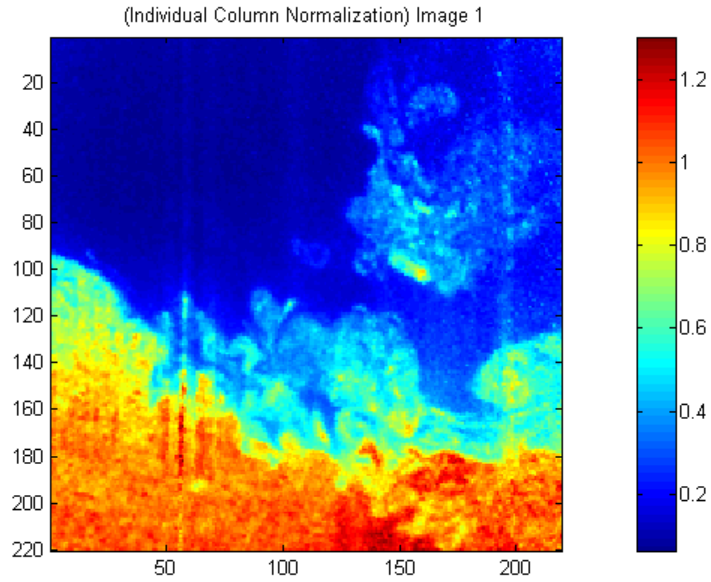
Figure 9: Image after column normalization technique is applied.
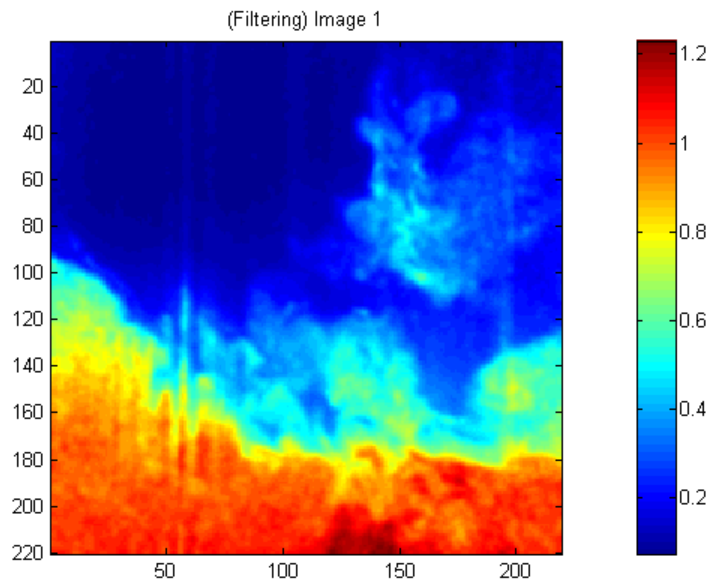
Figure 10: Image after smoothing filter is applied.

Figure 8 shows the image after the thresholding corrections have been applied. There is no difference between Figure 7 and Figure 8 that the eye can discern, but this correction is still useful because it removes spurious intensity values that might exist due to ambient light. Figure 9 shows the results of the column normalization technique. The

improvement in light sheet intensity throughout the entire image is evident, particularly in the lower layer where the intensity is nearly uniform. Of particular note is how the normalization technique was able to remove the local reductions in intensity mentioned earlier due to the spots on the mirror. While there are still some artifacts left over from this problem, the column normalization technique provided a vast improvement compared to Figure 8.

Figure 10 shows the image after the smoothing filter is applied. The filtering process helps to get rid of the imperfections left over after the column normalization technique. One thing this image cannot show is the results of the smoothing filter in 3-D. To effectively illustrate the 3-D results of the smoothing filter, an isosurface rendering of an entire 3-D sequence is given in Figure 11 before the smoothing filter is applied. Figure 12 is an isosurface rendering after the smoothing filter is applied.
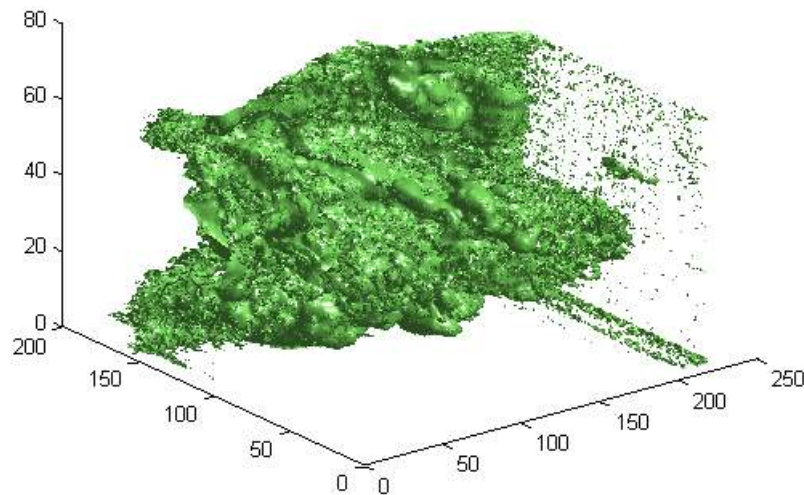

Figure 11: Isosurface rendering of a 3-D boundary layer edge before the smoothing filter is applied.
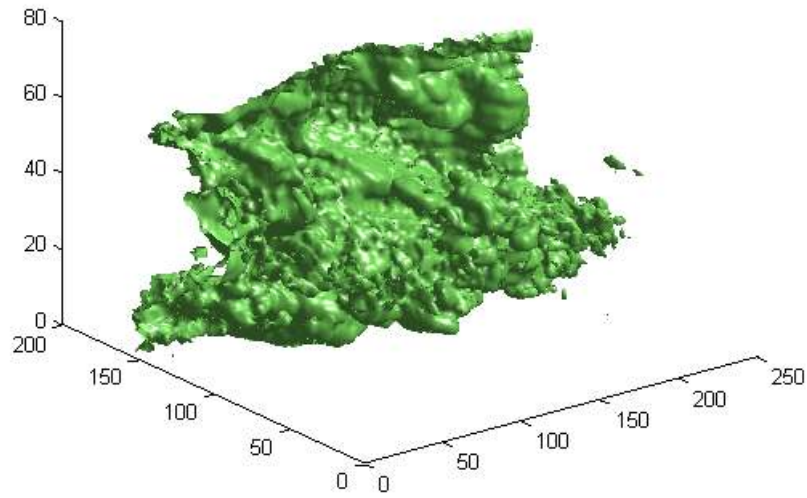
Figure 12: Isosurface rendering of a 3-D boundary layer edge after the smoothing filter is applied.

After all of these corrections, the 3-D matrix is converted to a Tecplot-compatible format and uploaded into Tecplot for rendering. Tecplot is capable of creating isosurface renderings as well as assembly views that show individual slices of the 3-D image on any of the three axes. The isosurface value is chosen by selecting the intensity value that most accurately traces the boundary layer edge. On average, there is about a 3-pixel area in which it takes the image to go from the uniform intensity in the boundary layer to the dark background in the freestream flow. This is less than 2% of the entire image, showing small variation in the ability to detect the boundary layer edge.

An important validation of the 3-D data involves analysis of the intensity of each image. It is expected that, on average, the intensity will be at a maximum near the wall and will slowly decrease as a function of boundary layer thickness. Then once the edge of the boundary layer is reached, the intensity should drop off dramatically. This ends up being exactly the case and is illustrated in Figure 13, with a dramatic drop in intensity

occurring right at the average boundary layer thickness. A velocity profile using the $1/7^{th}$

power law is also plotted to compare the average intensity trend with the average

velocity.
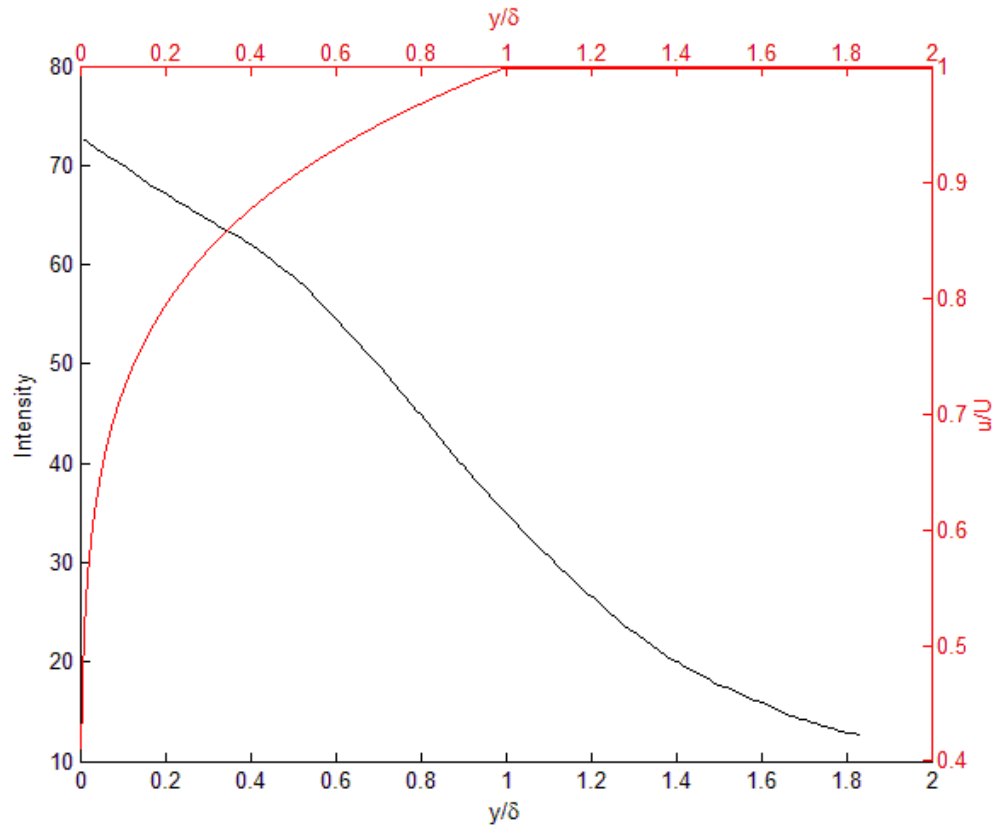
Figure 13: Average image intensity vs y/δ with velocity profile.

One other analysis that was done involved the standard deviation of the intensity

values at each y-location between all the images. If the smoke seeding method is

sufficient, maximum intensity fluctuations should occur near the boundary layer edge,

with minimal fluctuations at the wall. Again, this was found to be the case and a graph of

the standard deviation as a function of y/δ is given in Figure 14. It shows that maximum

fluctuations occurred at about y/δ = 1.0.

Figure 14: Standard deviation of intensity vs y/δ

4   EXPERIMENTS

4.1 General Components

There were some general components used in both the PIV and 3-D flow visualization experiments. These components are discussed below.

4.1.1   Wind Tunnel

The wind tunnel used is an Eiffel type open-circuit subsonic wind tunnel with test section dimensions of 2 feet in width, 2 feet in height, and 8 feet in length. It has a minimum speed of 11 feet per second and a maximum speed of 165 feet per second. Air is drawn into the inlet and travels throug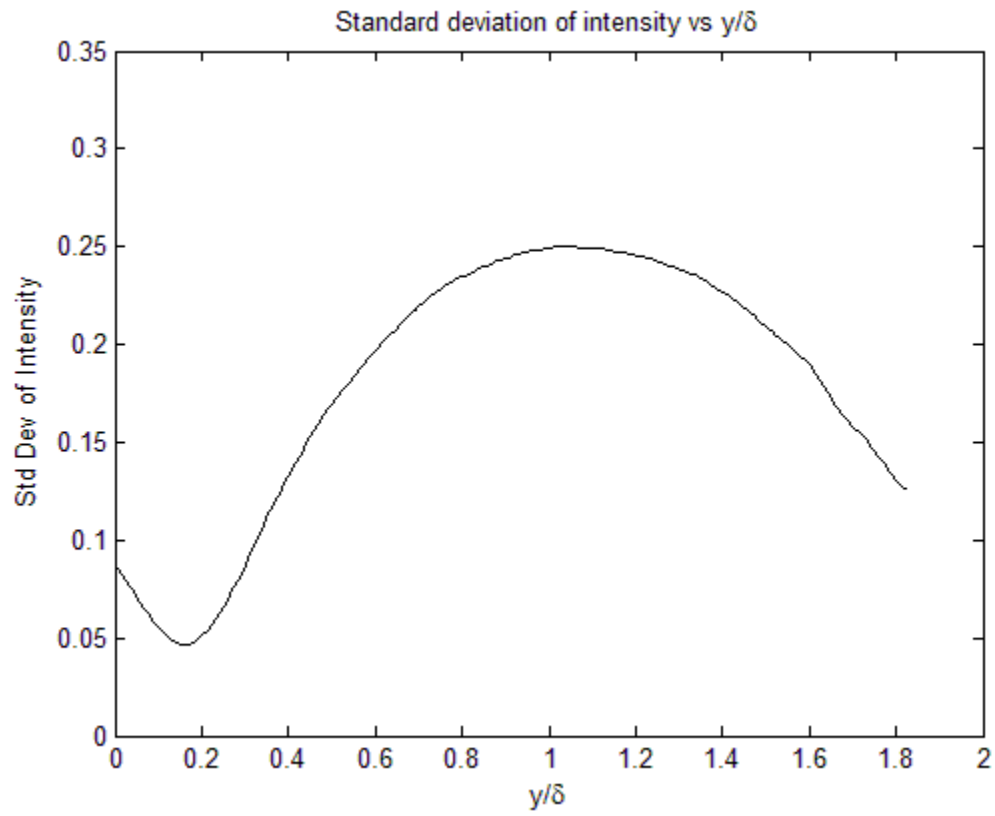h a honeycomb and screen pack, where it then accelerates through a contraction with a 6.25:1 area ratio and arrives at the test section. The air traverses the test section and passes through an axial fan (Joy Technologies, Inc. Model No. 38-21-1770CP) and diffuser where it is finally released into the atmosphere.

4.1.2   Flat Plate

A flat plate model was used for this research similar to previous models proposed by Roach and Brierley (1990) and Walsh et al (2005). It includes an elliptical leading edge to prevent separation at the leading edge and is declined at a 5 angle of attack with respect to the flow direction in order to achieve a negligible pressure gradient. Orienting the flat plate slightly downward with respect to the flow direction moves the stagnation point closer to the upper surface, creating lower pressure on the bottom of the flat plate

and reducing flow reversal on the leading edge. Similar techniques have been discussed by Roach and Brierley (1990) in which a trailing edge flap was used to achieve comparable results.[19] The flat plate is 92.5 inches in length which is sufficiently long enough such that we can look at boundary layers in a variety of sizes and conditions. For instance, we can visualize thicker turbulent boundary layers at the same velocity simply by acquiring images further down the length of the flat plate. Even more importantly, we can observe the physics of transitioning boundary layers at lower speeds than would be possible with a shorter length, which will come in handy for future research directions. For this thesis, our main benefit from the large length was that a thicker boundary layer allowed us to more easily define the large scale structures in the outer layer.

For flow seeding, a 1/8 inch-width slit was cut into the flat plate perpendicular to the flow at 4 inches of length at 18 inches from the leading edge. Particles from the smoke machine were introduced to this slit through a pipe originating from the particle reservoir discussed in 4.7.2. Following this slit 6 inches downstream was a strip of 50-grit sandpaper covering the span of the plate which was used to trip the boundary layer and induce turbulence. A description of the setup of the flat plate is shown in Figure 15.
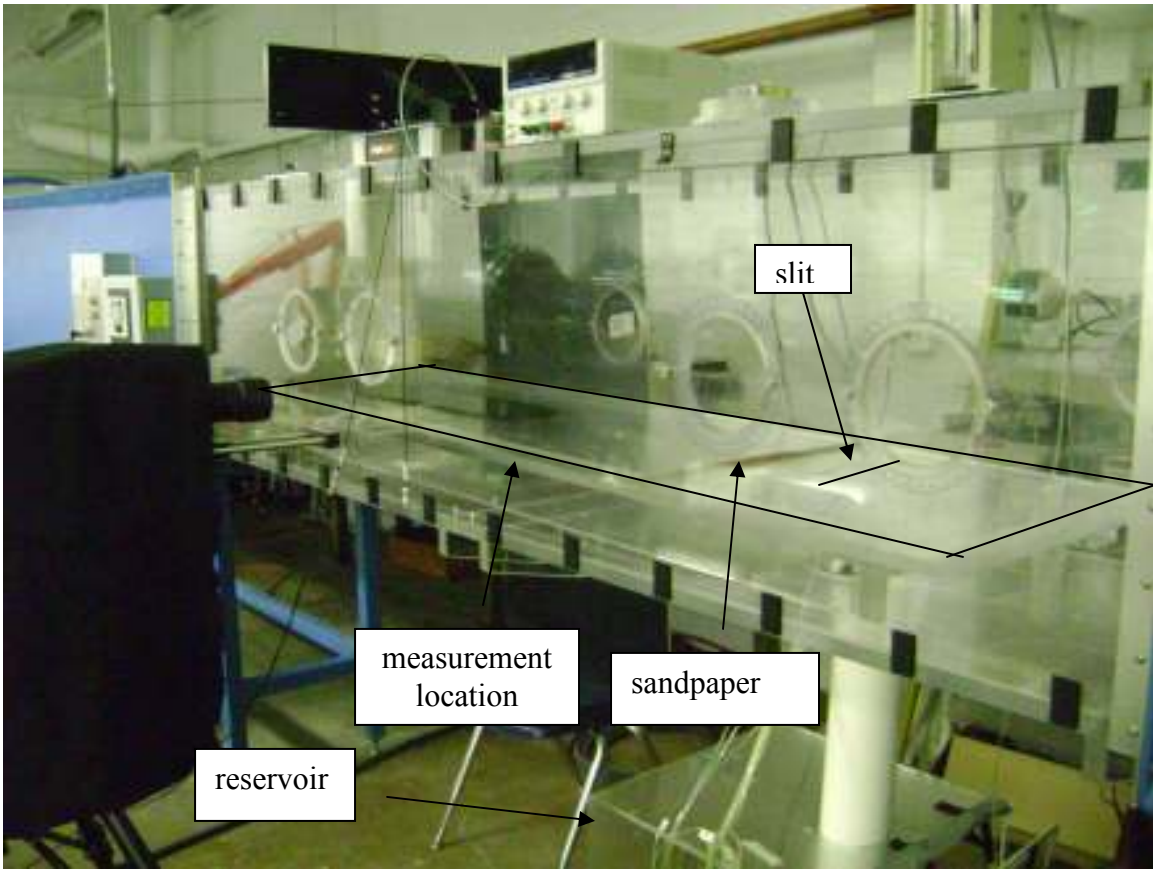
Figure 15: Description of the setup for the flat plate

4.1.3 Smoke Machine

The smoke machine used for the 3-D flow visualization and PIV experiments was a ViCount Compact 1300 oil-based smoke generator that produces particles 0.2-0.3 microns in diameter. The difference in application of the smoke generator in the two experiments is the seeding technique. For PIV measurements, the entire flow field was seeded with particles from the smoke machine by filling the room with particles and allowing the open-circuit wind tunnel to constantly recirculate the particles. For 3-D flow visualization, only the boundary layer was seeded with particles. The particles were conditioned by a reservoir where the vacuum from the wind tunnel test section pulls the conditioned particles through a slit in the flat plate. As a result, the particles remained

within the boundary layer as they traversed the plate. The reservoir is discussed in more detail in section 4.7.2.

4.2 Validation of Experimental Setup

There are many conditions that must be satisfied to ensure a proper and efficient experimental setup. For instance, it is pivotal that a zero-pressure gradient be maintained. Any objects added to the flat plate must be checked to ensure they have no effect or a negligible effect on the flow field, such as tripping mechanisms and slits for flow seeding. The PIV measurements should also be validated by comparing the resulting velocity profiles to profiles measured by other means. The experiments performed for these kinds of validations are discussed in this section. All of the following experiments were performed at an x-location of 5.5 ft with a freestream velocity of 100 ft/s, with the exception of the pressure gradient measurements, which were taken at the same freestream velocity but roughly 2 ft upstream from the original x-location.

4.2.1   Pressure Gradient Experiments

The goal of this thesis is to take measurements on a zero-pressure gradient turbulent boundary layer. As such, the pressure gradient must be measured to ensure these conditions. This was done by taking static pressure measurements from nine pressure taps spaced one inch apart in the streamwise direction on the flat plate. The location of these pressure taps were between 2 ft and 1 ft upstream of the volumetric visualization location. The measurements were taken using a Scanivalve 48D9-1106 pressure transducer which sent voltage measurements to a computer. The voltage

measurements were converted to a pressure reading based on a linear calibration curve. The pressure measurements were then saved to an Excel spreadsheet.

4.2.2   Results from Pressure Gradient Experiments

Pressure gradient measurements were taken for the flat plate mounted at -5 degree angle of attack with respect to the flow direction. Five runs were performed for this case and the value from each port was averaged. The results from these experiments are shown in Figure 16. The difference between the highest and lowest average measured static pressure for this case was 0.24%.
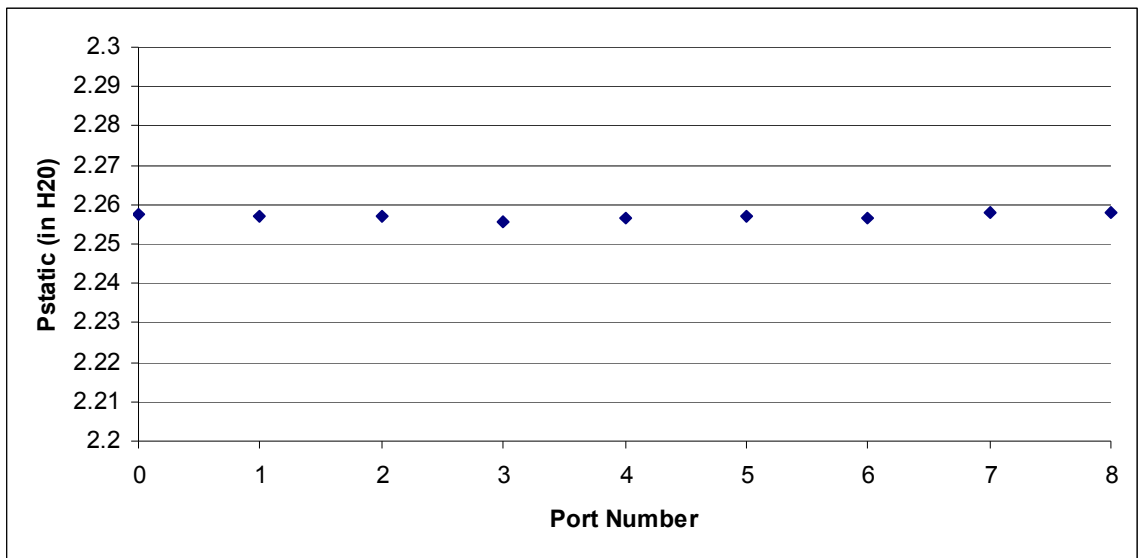

Figure 16: Static Pressure Measurements

4.2.3   Pitot Probe Experiments

Pitot probe experiments were conducted for comparison with the average velocity profile data from the PIV experiments. The probe was connected to a traverse that moved the probe at user-defined steps from the wind tunnel surface to the freestream. The pitot

probe measured stagnation pressure at each step and directed the measurements to a computer. Static pressure was measured from a port to the wind tunnel, and this value was subtracted from the pitot pressure measurement to get dynamic pressure and hence a velocity profile. The experiments were run five times for each test case and the velocity measurements were combined to get an average profile.

4.2.4   PIV Experiments

660 pairs of images were taken for the PIV experiments at the same location as the measurements for the pitot probe and 3-D flow visualization experiments. These image pairs were averaged to get an average boundary layer thickness for comparison to the expected values. It was envisioned that a 32 x 32 pixel region would be used for the initial correlation and that a 16 x 16 pixel region would be used for the following six-pass correlation in order to achieve satisfactory resolution. Hence, it was calculated that the required interpulse timing (discussed in 2.2.3.2) would be 15 μs. The PIV software used for this research is discussed in section 4.2.4.3.

Figure 17 gives a basic illustration of the experimental setup for the PIV experiments conducted for this thesis. A breakdown of each component specific to these experiments is described below.
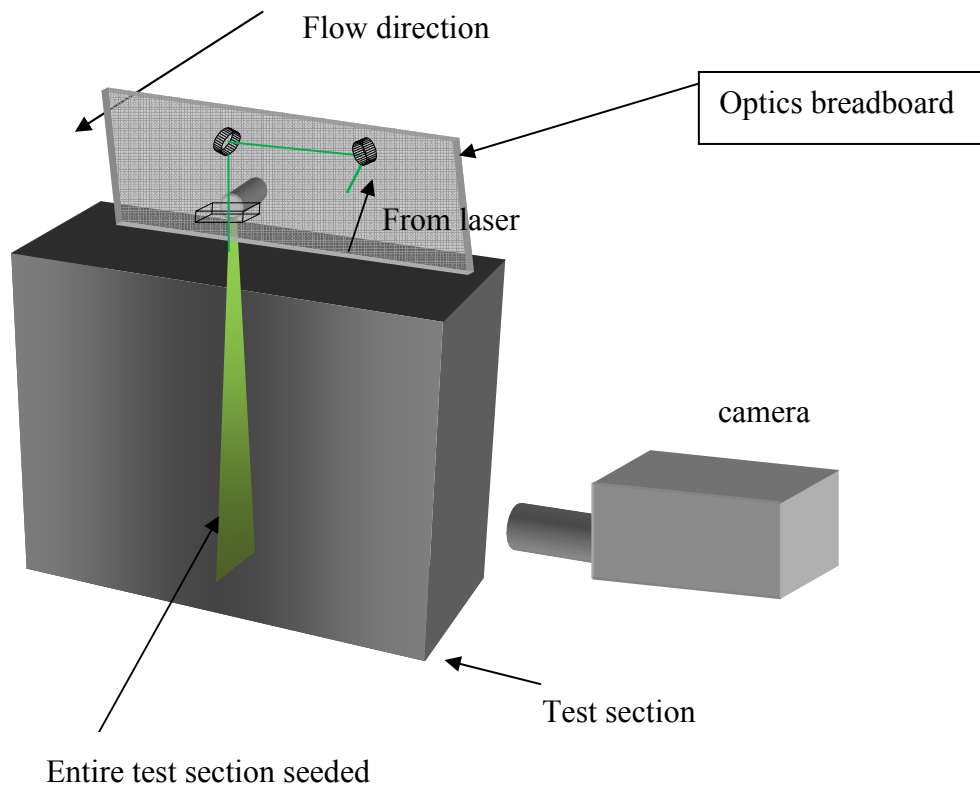
Figure 17: Schematic of PIV experimental apparatus

4.2.4.1 Laser

A New Wave Research Solo III PIV laser at a wavelength of 532 nm was used for the PIV measurements in this thesis. It has a repetition rate of 15 Hz and provides 50 mJ of energy per pulse with a duration of 3-5 ns. The laser includes onboard inputs and outputs for synchronization of the laser pulses with the optical setup. The laser pulses can be triggered internally by the "Rep Rate Knob" on the control panel of the laser. The pulses can also be triggered externally by three different means: Q-switch triggering, flashlamp triggering, and TTL direct triggering. For these experiments, TTL direct

triggering was used so that the pulses from the laser could be controlled by the same pulse generator that commands the camera to fire, making synchronization easier.

4.2.4.2 Camera and Software

The camera to be used in this experiment is a Cooke Corp. Sensicam QE Doubleshutter 12 bit CCD camera. It has a maximum resolution of 1376 x 1040 pixels and a maximum frame rate of 10 frames per second. The exposure time, resolution, frame rate, and other parameters can be set via the CamWare V 2.19 software. The camera was externally triggered using a pulse generator

4.2.4.3 PIV Software

The PIV software used in this thesis is called PIVPROC. It is a program provided by NASA Glenn Research Center to Auburn University for educational purposes. The program can load a pair of images or a sequence of pairs for batch processing. It produces a vector field based on user-specified values such as interrogation region and number of iterations in a multi-pass correlation. A view of these settings is shown in Figure 18.
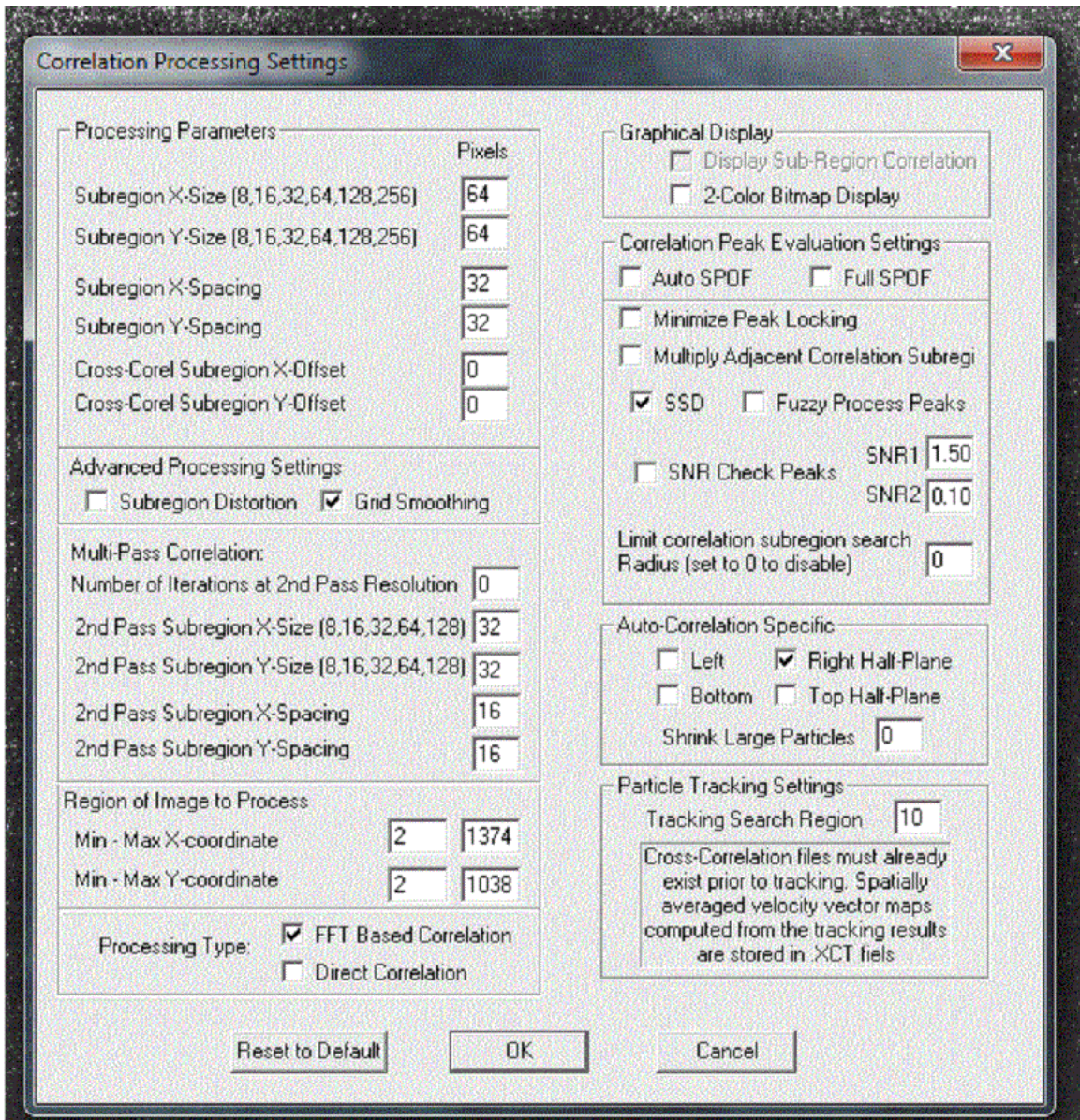
Figure 18: Correlation processing settings from PIVPROC.

Based on the setting shown in Figure 18, the image pair is initially processed in 64 x 64 pixel subregions, with the subregion spacing being the distance between adjacent subregions. For this research, a 32 x 32 subregion spacing was used. For the multi-pass correlations, a 64 x 64 pixel subregion was used again, but a 16 x 16 subregion spacing was used for increased resolution. For these experiments, six iterations were performed

using FFT-based correlation with grid smoothing and subregion distortion. Grid smoothing uses a peak removal algorithm which removes vectors lying a far distance away from its surrounding eight neighbors and replaces them with an interpolated value. Subregion distortion uses local velocity gradient values to distort the subregion before performing correlations in order to reduce the bias introduced by these velocity gradients.

4.2.5 Velocity Profiles from Pitot Probe and PIV Measurements

Expected values for boundary layer thickness, displacement thickness, and momentum thickness were calculated before the PIV and pitot probe experiments using empirical formulas derived for a flat plate turbulent boundary layer. Those calculations are shown in Table 1, with the equations used for these calculations shown here.

$$\delta = \frac{0.37x}{\sqrt[5]{\mathrm{Re}_x}} \qquad\qquad \delta^* = \frac{\delta}{8} \qquad\qquad \theta = \frac{7}{72}\delta$$

Table 2 gives the results from the PIV and pitot probe measurements, while Figure 19 shows the non-dimensionalized boundary layer profile compared to the 1/7th power law profile.[20] The results from the two measurement techniques were very comparable, with all of the values being very close to what was expected. One noticeable difference in the boundary layer profile for the pitot probe data in Figure 19 is the shape from the bottom to about $y/\delta = 0.5$. The reason the shape deviates from the other results is the nature of the pressure transducer used for the pitot probe measurements. The transducer calibration procedure uses a linear calibration over a small window of pressures, but this calibration is not as accurate outside of the small window in which the calibration was performed. The pitot probe was calibrated for a range of 75% to 100% of freestream pressure. Hence, the data closer to the wall (where pressures are much lower

in comparison) was not as accurate. Using a pressure transducer with a wider range of operation would have yielded a closer fit, but one was not available at the time of these experiments. A plot of the boundary layer profile from pitot probe and PIV data in absolute units is given in Figure 20 to show that the two measurements did in fact measure similar boundary layer thicknesses.

One other factor to be taken from the plot in Figure 19 is that the $1/7^{th}$ power law profile is a mean profile for turbulent boundary layers in moderately favorable pressure gradients.[21] The fact that the data (particularly the PIV data) closely follows this model gives some evidence that this flow field was not in the presence of an adverse pressure gradient. Additionally, the shape factor, $H = \delta^*/\theta$, for this flow is 1.29, which matches the theoretical value for the shape factor of a boundary layer with no pressure gradient. Comparatively, separation for a turbulent boundary layer occurs at a shape factor between 2.2 and 2.4. This fact coupled with the relatively low wall shear stress calculated in section 5.1 provides even further validation of the absence of an adverse pressure gradient.[22]

U (ft/s)	x (ft)	Re_x	Expected			
			δ (in)	δ^* (in)	θ (in)	Re_θ
100	5.5	3300000	1.21	0.150	0.120	5889

Table 1: Expected boundary layer values from experiments

Technique	Measured			
	δ (in)	δ^* (in)	θ (in)	Re_θ
PIV	1.21	0.151	0.117	5870
Pitot	1.21	0.166	0.118	5888

Table 2: Measured boundary layer values from PIV and pitot probe experiments
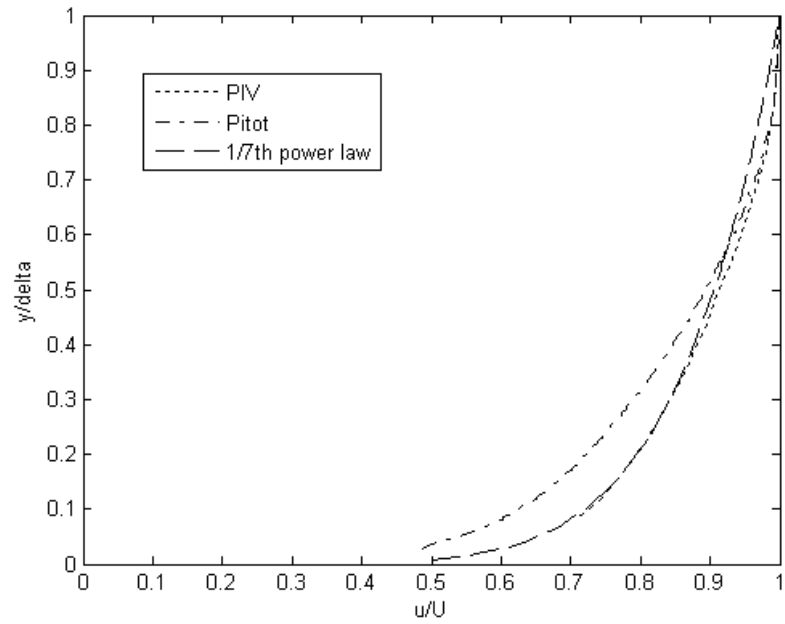
Figure 19: Results from PIV and pitot probe measurements for average boundary layer thickness.
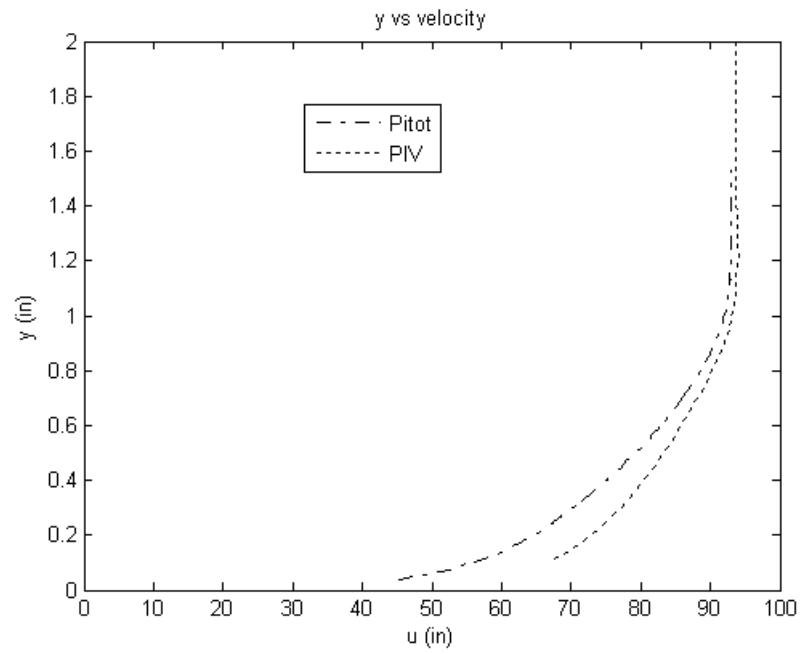

Figure 20: Results from pitot probe and PIV measurements in absolute units.

56

4.3 Components and Setup for 3-D Flow Visualization

The 3-D flow visualization experiments were taken at a freestream velocity of 96
ft/s and an x-location of 5.5 ft (matching the experiments above). Figure 21 gives a basic
illustration of the experimental setup for the 3-D flow visualization experiments
conducted for this thesis. A breakdown of each component and method used specifically
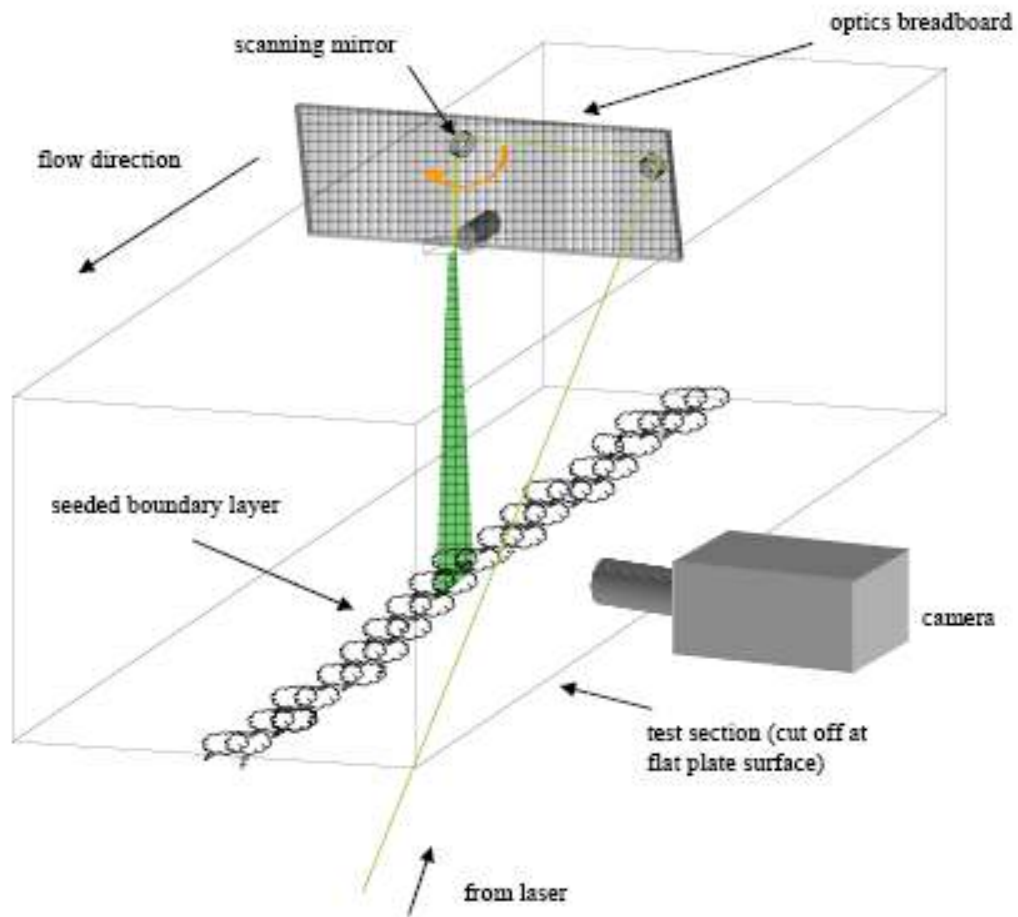for these experiments is described in this section.

Figure 21: Schematic of 3-D flow visualization experimental apparatus

4.3.1   Laser, Camera, and Software

The pulse burst laser in the Auburn University Advanced Laser Diagnostics Laboratory was configured to create bursts of 68-pulse trains at 532 nm wavelength and 20 nanosecond duration. Figure 22 gives a description on the scanning technique used by the laser. The laser light passed through a positive lens to focus the laser beam and was followed by a rectangular plano-concave lens to form the laser beam into a sheet. The mirror rig sat on top of the wind tunnel and was pointed downward as shown in Figure 21. A scanning mirror was used to deflect the light across the flow field, and a camera was synchronized to take an image at each pulse, allowing a volumetric resolution of the flow field. The camera interfaced directly with a computer and utilized provided software in order to produce a sequence of images. These sequences were then uploaded into a MATLAB code and converted to a Tecplot-compatible format. The sequence was then reconstructed as a 3-D plot.
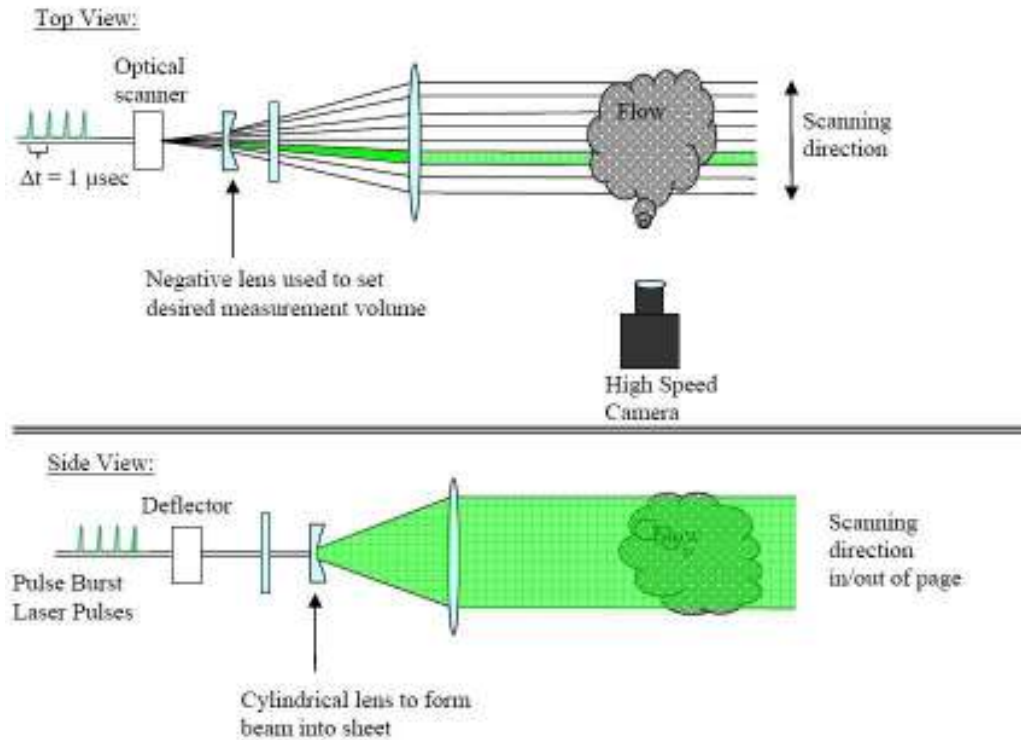
Figure 22: Description of scanning technique for 3-D flow visualization (Lynch and Thurow 2008).

4.3.2   Reservoir

In order to condition the smoke particles, a reservoir in the form of a simple box was used. The smoke machine was situated at one side of the reservoir with a hole cut into the face to introduce the smoke. The opposite face had a larger hole cut into it which held a PVC pipe that leads to the wind tunnel test section and connected to the slit in the flat plate as discussed in the next section. The reservoir acted as a settling chamber and the smoke particles were pulled through the PVC end of the reservoir due to the vacuum from the test section.

5   EXPERIMENTAL RESULTS

5.1 Results from PIV Experiments

All 660 image pairs from the PIV experiments were averaged together to derive some statistics of this flow field. Specifically, plots of friction velocity, Reynolds stresses, and velocity profile are given to show that the trends of these values are what are seen in a typical zero-pressure gradient turbulent boundary layer. For information on how these values were derived in MATLAB, refer to Appendix C.

The friction velocity value for these experiments was calculated using a technique described by Kendal and Koochesfahani.[23] This technique utilizes a Spalding profile for the log region of the boundary layer to iterate for the friction velocity.[24] This technique is illustrated in Figure 23, with the formula for the Spalding profile given below.

$$y^+ = u^+ + \exp(-\kappa B)\left[\exp(\kappa u^+) - 1 - \kappa u^+ - \frac{(\kappa u^+)^2}{2} - \frac{(\kappa u^+)^3}{6}\right]$$

Values for κ and B were taken to be 0.41 and 5.0, respectively, and are values typically used for turbulent boundary layers. The result of this technique revealed a friction velocity of 3.78 ft/s and a wall shear stress of 2.36×10^{-4} psi.
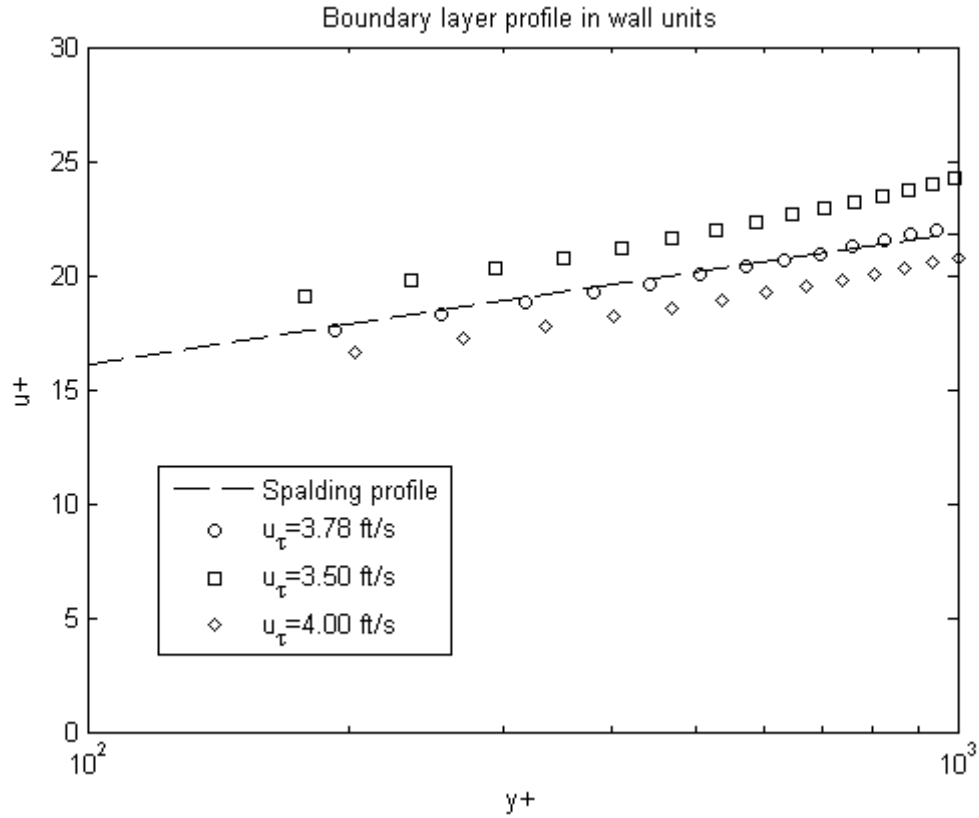
Figure 23: Graph of different friction velocity values used to fit the PIV data to the Spalding profile.

Figures 24-26 show plots of the Reynolds stress components $\langle u'\rangle^2$, $\langle v'\rangle^2$, and $\langle u'v'\rangle$ as a function of y+. This Reynolds stress is normalized by the friction velocity computed in the previous graph. Trends from these graphs follow values computed by previous research on turbulent boundary layers with no pressure gradient.[25,26] Figure 27 is a plot of the velocity profile of the data compared to the velocity defect law. Again, the two profiles closely match each other.

Figure 24: Plot of Reynolds stress component <u'>^2.
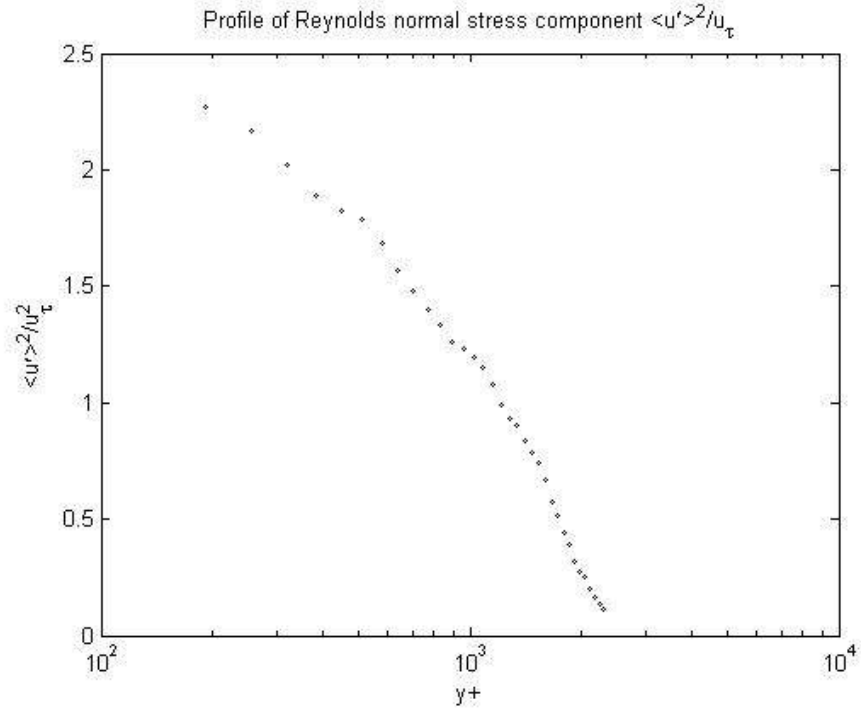

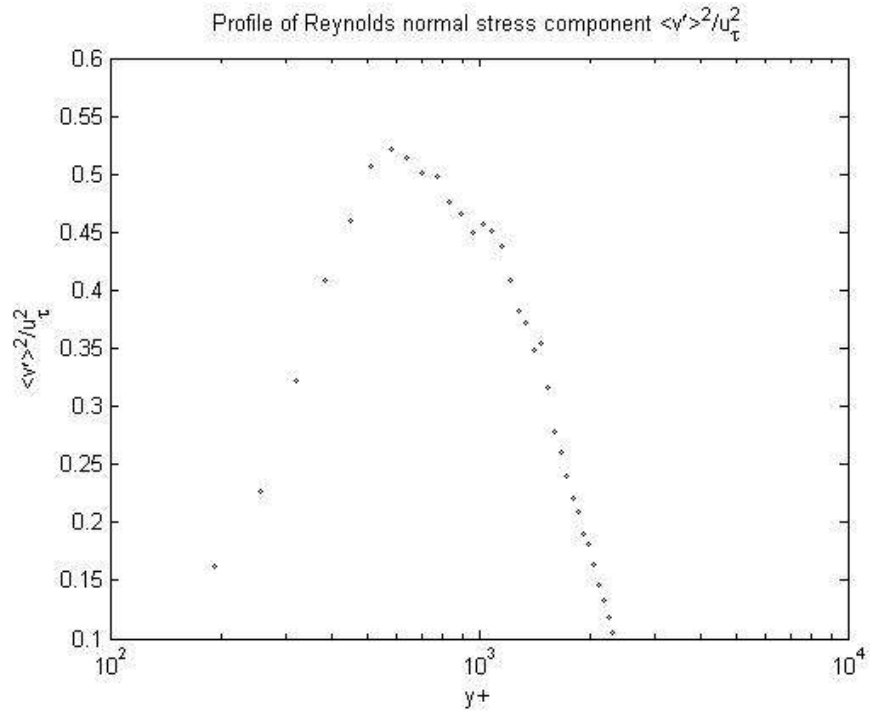**Figure 25: Plot of Reynolds stress component <v'>^2.**

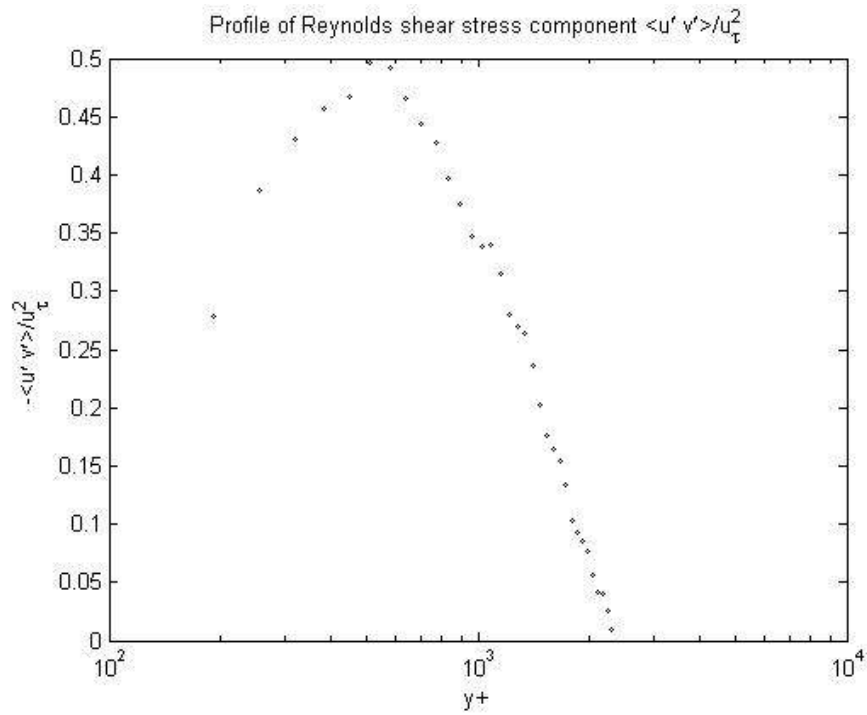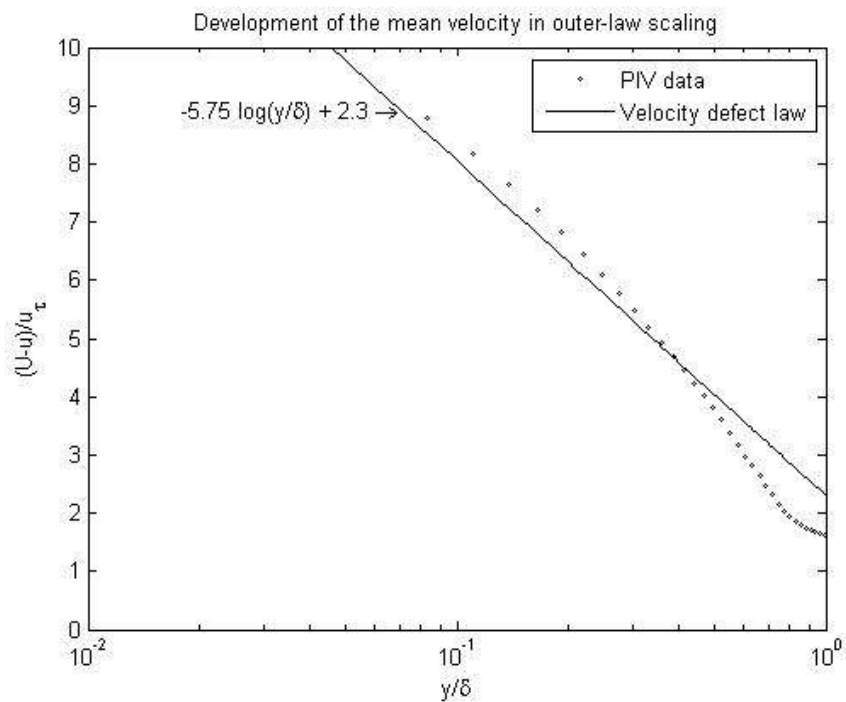**Figure 26: Plot of Reynolds stress component <u'v'>.**

Figure 27: Plot of boundary layer profile from PIV data in comparison to the velocity defect law.

63

Figure 28 presents the contour plot of the averaged values from the PIV data. The contour plot shows that the mean profile is slightly less than one inch thick, but as shown in section 4.2.5, the actual thickness measured from the averaged PIV data is 1.21 inches. The discrepancy is due to the method used by MATLAB to plot the contours. It cut the value off abruptly at 5% less than the freestream velocity value. Regardless, the main purpose of this figure is to illustrate the strong results of averaging 660 images.
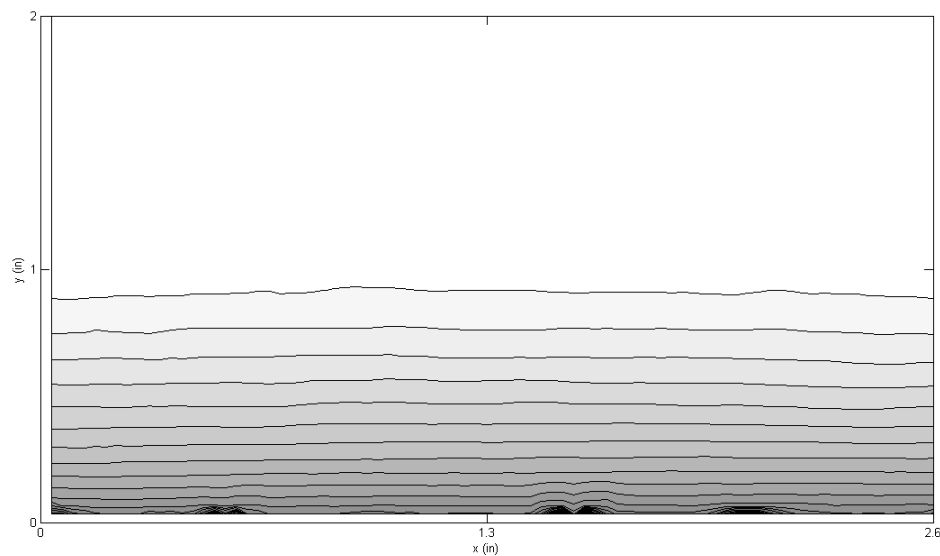
Figure 28: Contour plot of velocity of averaged PIV data.

The following images are the result of PIV measurements from individual image pairs that showed some interesting features. These images are mainly included as a comparison to the data presented by Adrian (2000) to further validate the experiments done for this thesis. The field of view for these images was 2.6 in x 2 in. Following a technique discussed by Adrian, 80% of the freestream velocity value was subtracted from the u component of velocity in order to reveal these structures in a quiver plot. In order to more easily visualize the structures that extend outward, resulting values of the

64

momentum layers were mapped on a contour plot. Figures 29-32 show the results of both of these techniques.

The heads of the large scale structures in Figures 29 and 31 have some striking similarities to the vortex heads discussed in Adrian (2000). The bodies of these structures are generally inclined at 45 degrees with respect to flow direction, like structures A and C, but in some cases the structures are inclined almost perpendicular to the flow direction, such as structure B. Another interesting feature is how convoluted the boundary layer edge appears. The momentum contour plots (Figures 30 and 32) show this feature particularly well, with pockets of freestream velocity dipping down to 0.25 inches from the wall in Figure 32.

Figure 29: Quiver plot of the resulting velocity data from one image pair taken in PIV experiments. Velocity values were subtracted by 80% of the freestream value in order to reveal vortex heads.

Figure 30: Contour plot of regions of constant u momentum in the boundary layer visualized in Figure 29.
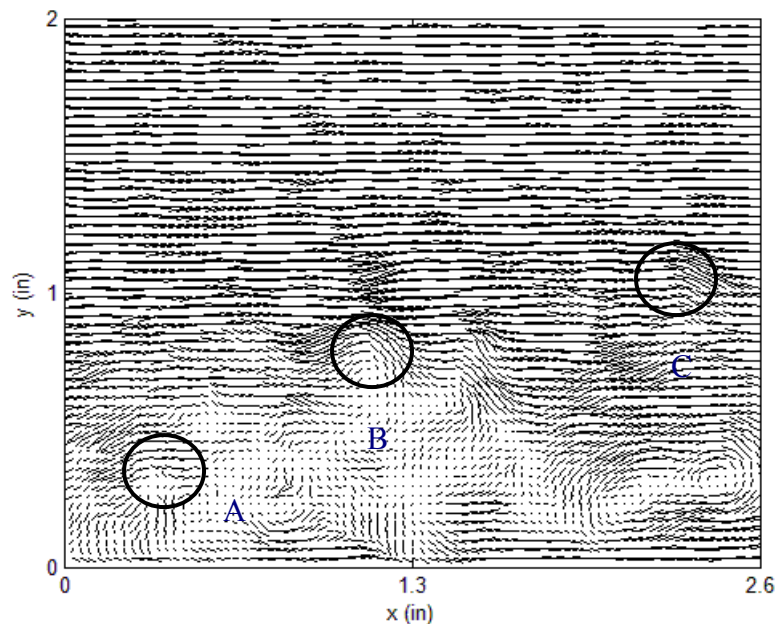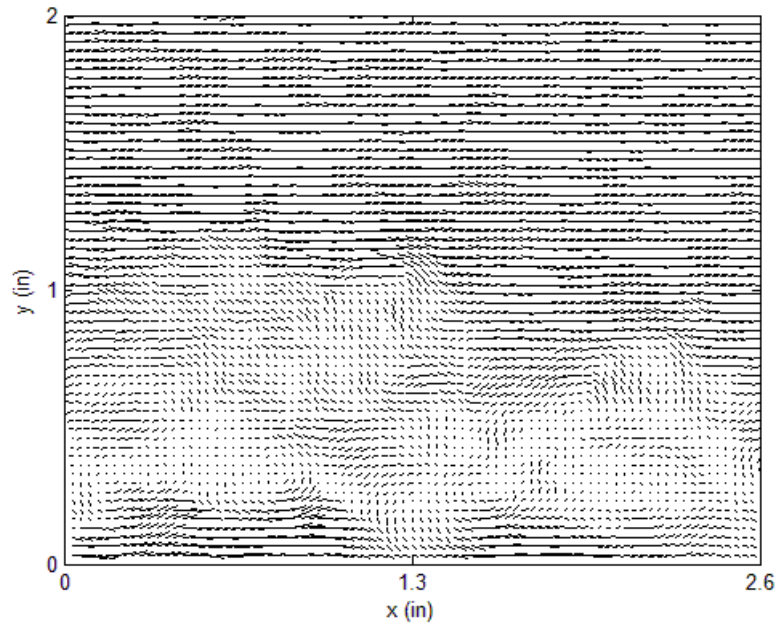

Figure 31: Quiver plot of the resulting velocity data from one image pair taken in PIV experiments. Velocity values were subtracted by 80% of the freestream value in order to reveal vortex heads.
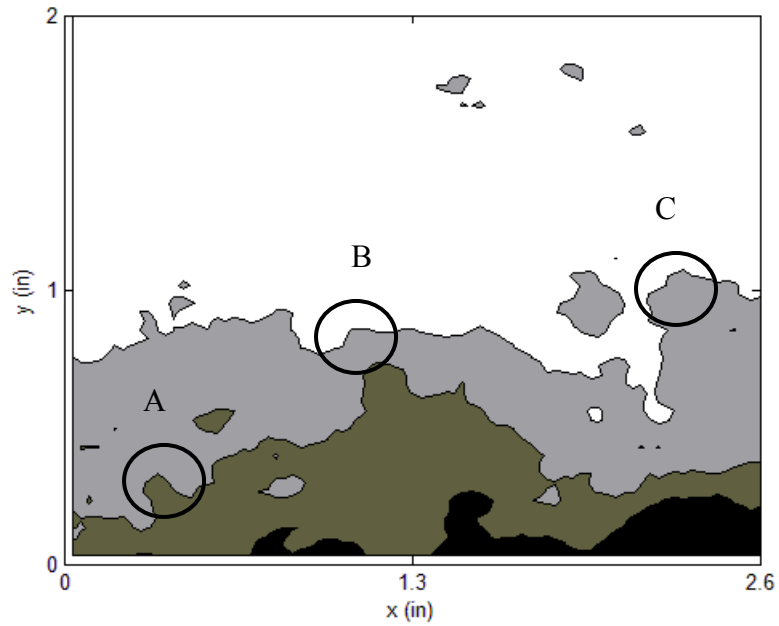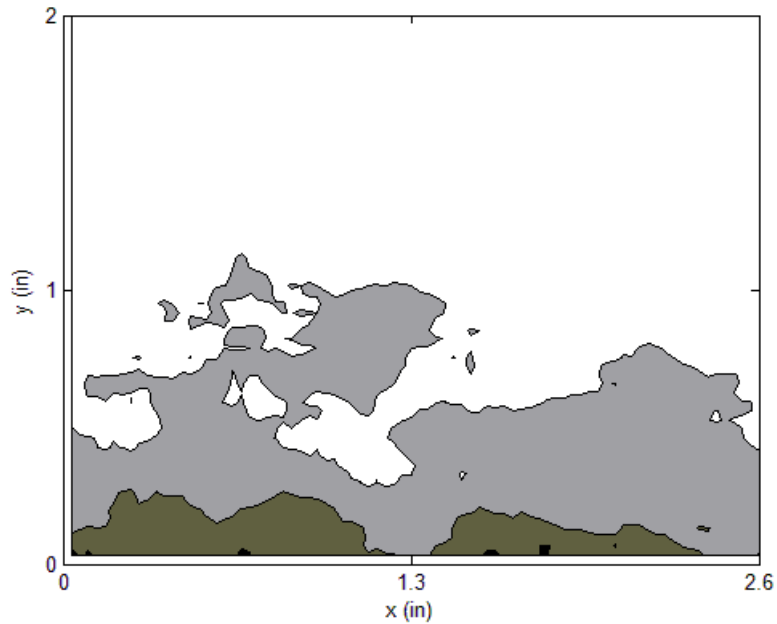
Figure 32: Contour plot of regions of constant u momentum in the boundary layer visualized in Figure 31.

5.2 Results from 3-D Flow Visualization Experiments

300 image sequences were taken for the 3-D flow visualization experiments. Some of the images are presented here, with many other images given in Appendix C to supplement this section. The field of view for each volumetric realization was 2 in x 2 in x 2 in. The large-scale structures would sometimes extend slightly outside the field of view in the y-direction. This occurred in roughly 60 of the 300 images, or 20% of all 3-D images. Structures as large as a boundary layer thickness in length and width were observed and had varying shapes ranging from cylindrical shapes to large bulges. The structures were inclined at many various angles with some of the larger structures appearing to be inclined at about 45 degrees with respect to flow direction. Collections of smaller structures often appeared in packets that extended out of the outer layer like fingers as is seen in Figure 33. Some larger structures extended outside the outer layer,

67

sometimes extending itself longer than an average boundary layer thickness. Isosurface renderings revealed a highly-convoluted boundary layer edge in many of the images, with deep recesses in the boundary layer occurring frequently. Other images appeared much less active, showing a less convoluted boundary layer edge with comparatively smaller structures, demonstrating the diversity of this flow field. Some examples of these phenomena are presented throughout this section in detail.

Figure 33 shows different views of a volume with the flow travelling in the negative x direction (this is a consequence of the experimental arrangement). Large-scale structures can be clearly seen at the outer edge of the boundary layer with the isosurface renderings shown in 33a-d. The intensity values for the isosurfaces were set to be the intensity value at the outer edge of the boundary layer in order to trace the edge. Figures 33c and 33d give two different zoomed views of a couple of interesting structures inclined at 45 degrees to the flow direction. The structures circled are of the smaller scale seen in the 300 images. They extend from the main body of the boundary layer to about 0.3δ in the streamwise direction. Many structures like these were revealed in the 300 sets of 3-D data and will be presented in later figures. Figure 33e illustrates the pulse scanning technique used to acquire the volumetric data, with every fourth pulse shown. It is worth noting that the intensity values in these images do not necessarily reflect the ongoing physics of the boundary layer. They are simply values representing the light intensity in the image.
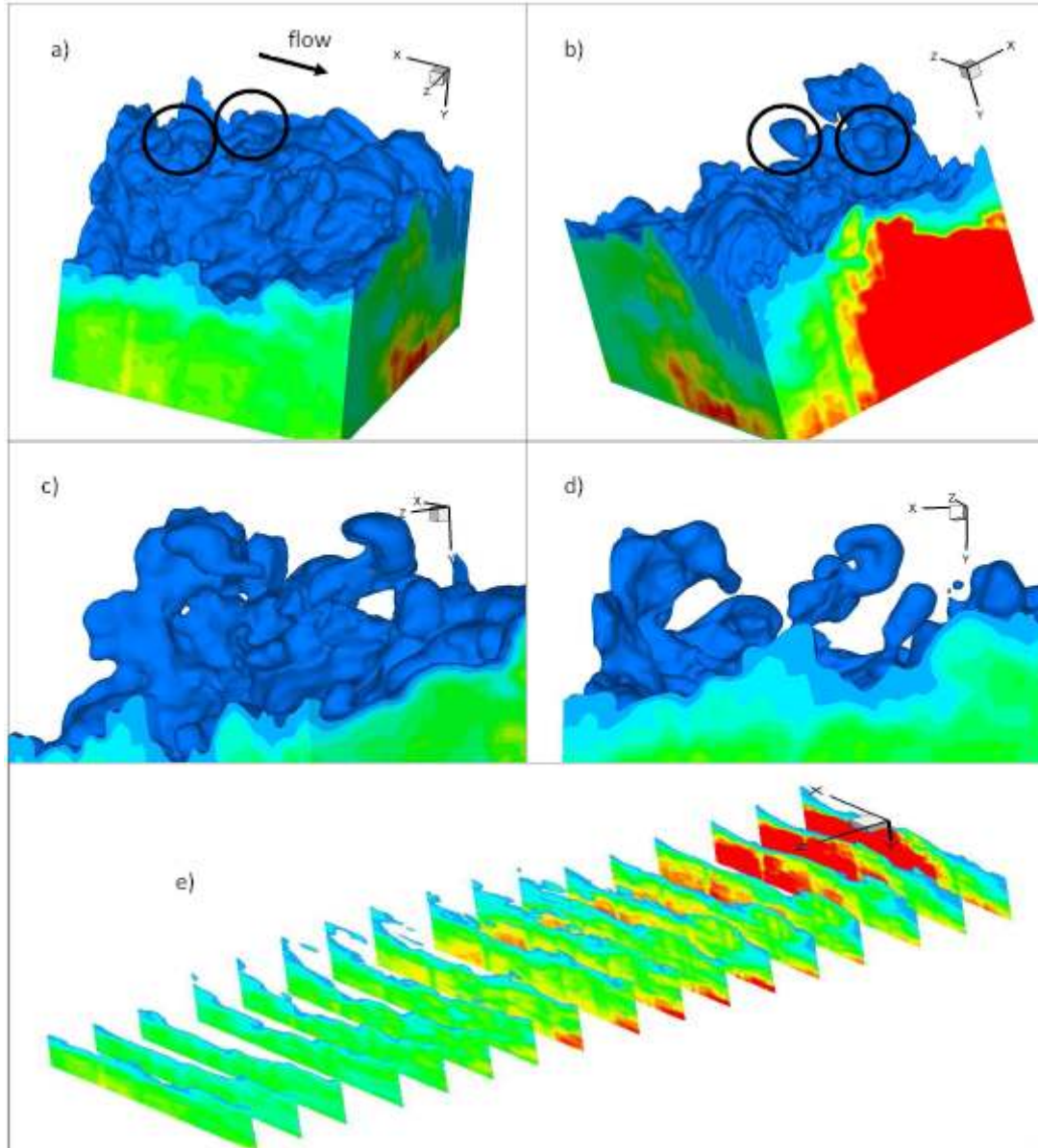
Figure 33: 3-D visualization of a boundary layer at $Re_0 = 5900$. Interesting structures circled in a) and b) and zoomed in for a better view in c) and d). Pulse scanning technique revealed in e) showing every fourth pulse.

Figure 34 gives a good example of one of the larger structures that extends outside the field of view. It is inclined almost perpendicular to the flow much like what was seen previously in the PIV data. The edge of the boundary layer appears more convoluted than what was typically seen in Figure 33, with clear evidence of this appearing in the left side of 34b in the form of a dramatic drop in boundary layer

thickness in the spanwise direction of about 0.5δ. Figure 34b gives a closer view of the large structure from another reference point and shows that this is actually not a contiguous structure but instead a collection of several columns of fluid extending into the freestream. This structure extends from the main body of the boundary layer and stretches just outside the field of view in the y-direction. It has a total length on the order of a boundary layer thickness and is about 0.5δ wide in the spanwise direction. To illustrate that this structure is not an artifact of the image post-processing procedure, an image of the 30th pulse in the raw data is presented in Figure 35, with the circled area being the structure in question.

Figure 36 shows a smaller finger-like structure looping out of the boundary layer nearly perpendicular to the flow direction, zoomed in at 36b to give a closer look. To the left of this structure is a collection of smaller structures erupting from the outer layer. Together, these structures make a large packet spanning about 0.3δ x 0.3δ x 0.3δ.
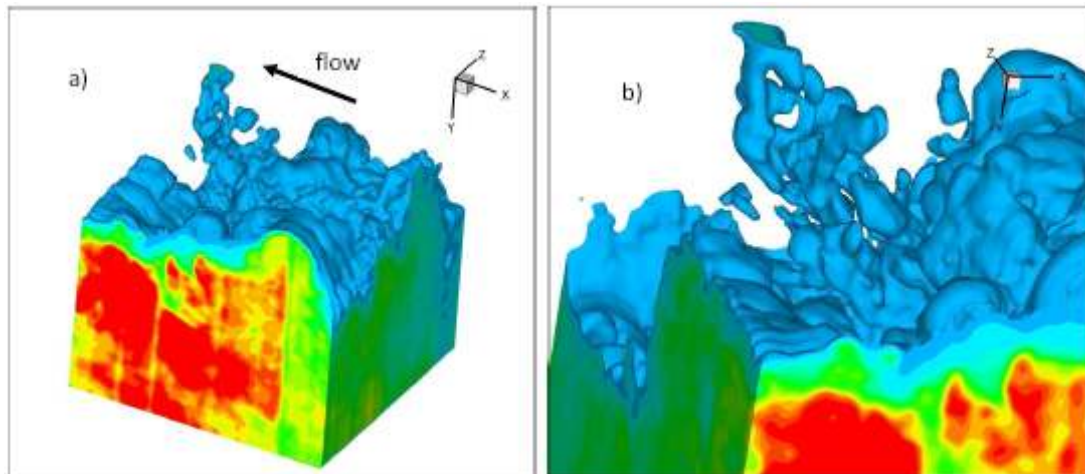
Figure 34: Turbulent boundary layer at Re_θ = 5900: a) an interesting structure can be seen extending beyond the field of view, b) zooming in and turning the volume reveals more interesting characteristics of this structure.
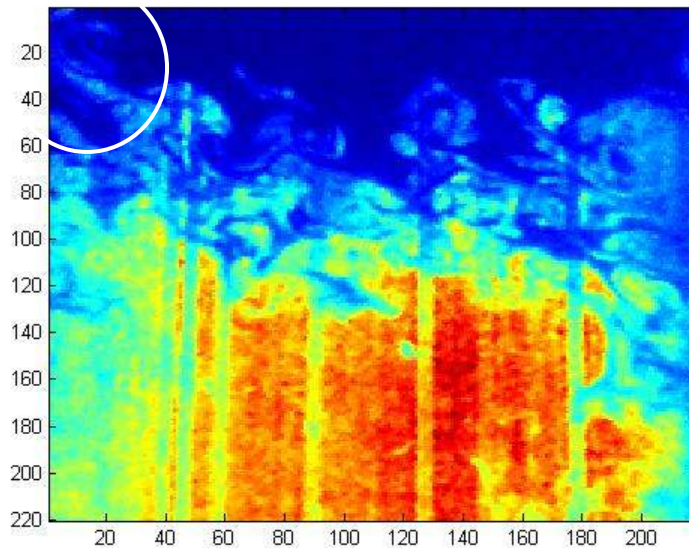
Figure 35: Raw 2-D image of realization from Figure 34, with large structure circled.
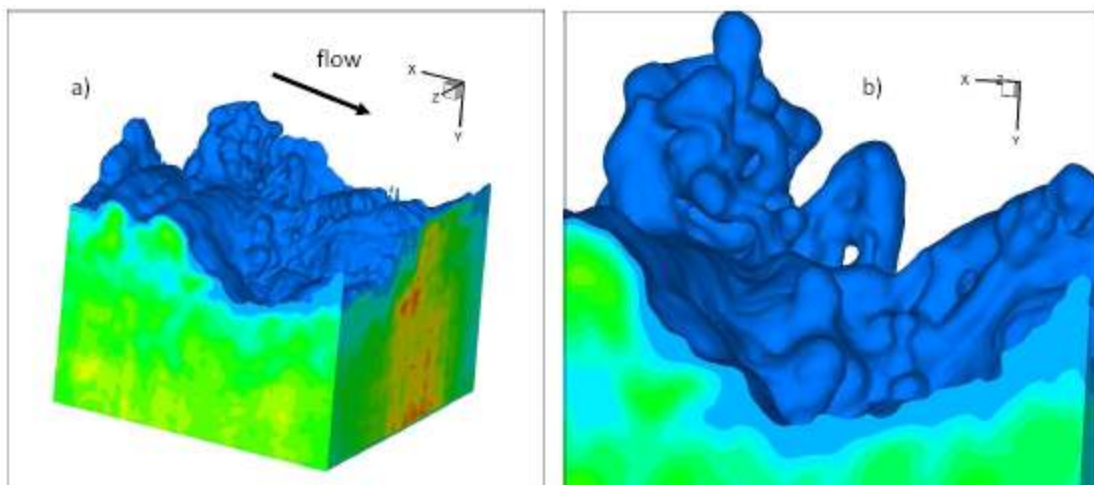
Figure 36: Another interesting structure from a turbulent boundary layer at Reθ = 5900, zoomed in at b).
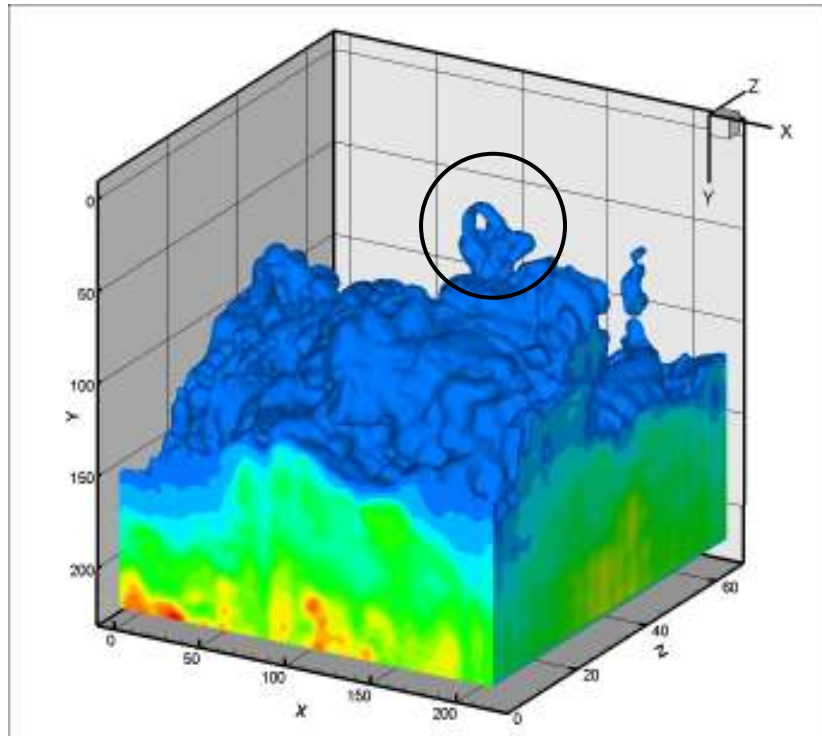
Figure 37: Another realization of a turbulent boundary layer at $Re_0 = 5900$.
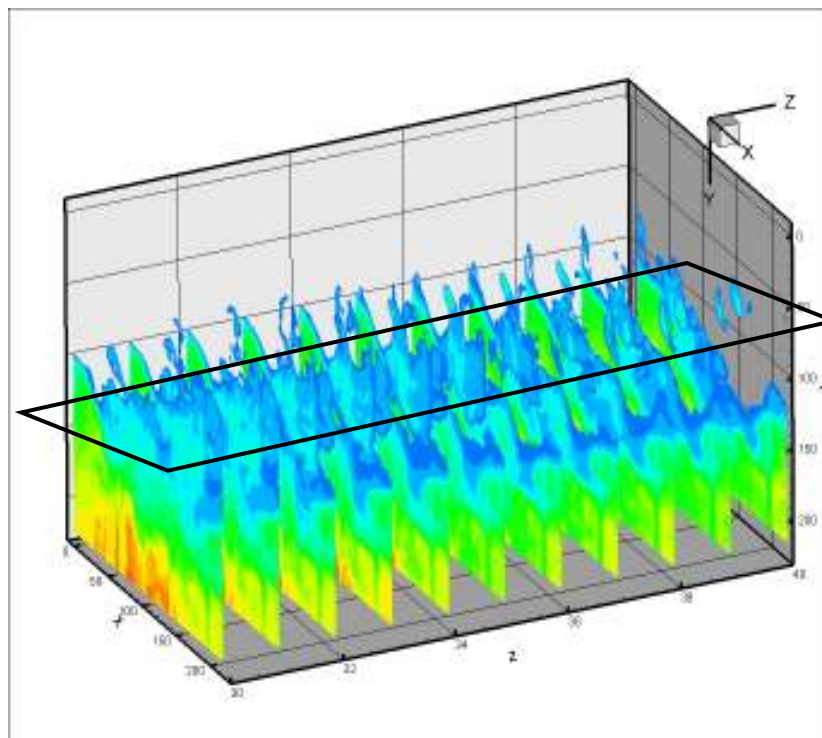
Figure 38: A spanwise illustration of the image shown in Figure 37.

Figure 37 is another 3-D image from this type of boundary layer. The axes displayed on this figure show the 220 x 220 x 68 pixel volume, with the z-axis scaled appropriately to create the cubic volume investigated in the experiments. A looping structure can be seen coming out of the outer edge of the boundary layer oriented nearly perpendicular to the flow direction. Other smaller structures can be observed throughout the boundary layer edge as seen in previous images.

Figure 38 is a pulse-by-pulse representation of the same volumetric data as shown in Figure 37 in order to show the spanwise shape of the structure discussed above. The structure was first visualized at the 30th pulse and died out at the 40th, giving it a total spanwise length of about 0.3δ. At the 30th pulse the structure is nearly cylindrical with a radius of roughly 0.2δ. Traversing the spanwise direction, the radius decreases and then appears to branch into two legs at the 38th pulse.

It is also important to illustrate the continuity between data resolved using Tecplot and data resolved using other software. Very recently a program called ImageVis3D was discovered by a student in the Auburn University Advanced Laser Diagnostics Laboratory. It is a freeware program developed by the University of Utah and is typically used in a biomedical setting. With the data from these experiments, a sequence of images saved in TIFF format can be uploaded into ImageVis3D, where it then compiles the images into one 3-D image. It has a built-in isosurface rendering function that draws an isosurface based on an isovalue. This isovalue is initially automatically set by the program but can be modified by the user. Figure 39 gives an example of an isosurface rendering of a particular 3-D image from the experiments. Figure 40 is the same image

rendered in Tecplot. It is evident that the details of the boundary layer, such as the shape and size of the outer layer and the structures, remain the same.
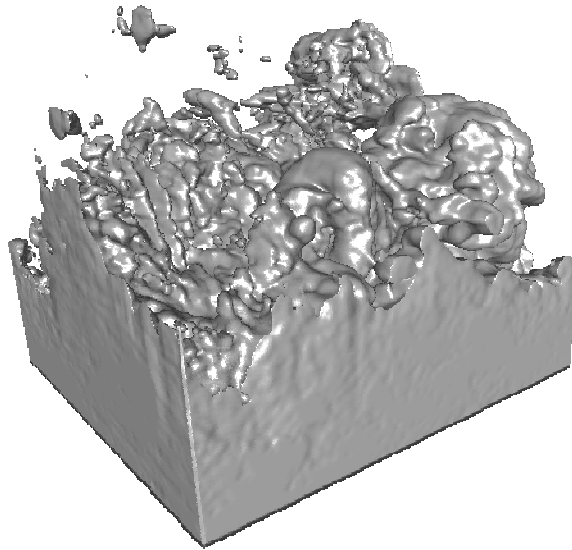
Figure 39: Isosurface rendering in ImageVis3D of a 3-D dataset from experiments.
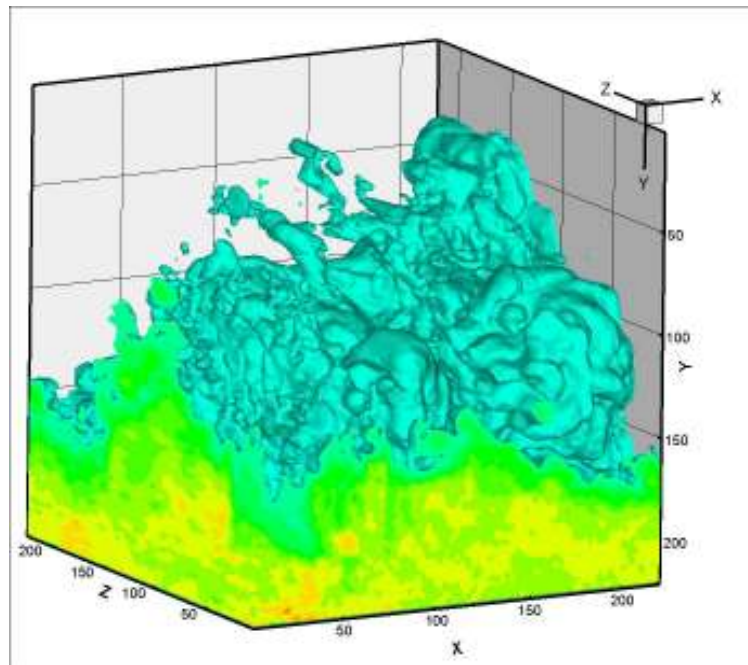
Figure 40: Isosurface rendering in Tecplot of the same 3-D dataset in Figure 39

5.3 Discussion

The 3-D images showed features that would be expected in a turbulent boundary layer, namely the convoluted nature of the boundary layer edge and the high variability in the size and shape of the structures in the outer layer. Since only one similar work had been done previous to this one (and at a Reynolds number one order of magnitude lower than this research) it is difficult to draw comparisons between the two. Experiments at different flow speeds and varying pressure gradients would be helpful in order to note the changes in the boundary layer, such as differences in scales of the structures in the outer layer.

It is tempting to make a connection between some of the structures seen in these images and the famous hairpin vortices that have become the focus of research in turbulent boundary layers. Due to the preliminary nature of this research as well as the qualitative nature of this visualization technique, care must be taken to not draw these connections without further experiments in a variety of flow conditions.

It would also be helpful to be able to quantify the 3-D data in some way, perhaps by simultaneous PIV and 3-D flow visualization measurements. This would likely involve taking the 3-D measurements using the pulse scanning technique and then immediately taking a 2-D PIV image in the center of the volume. The key to this technique would be that the 2-D slice for the PIV data would have to coincide with a structure resolved by the 3-D data in order to quantify the structure. This would obviously be a "hit-or-miss" technique that would likely take many measurements to get one desirable data set. To this end, 3-D PIV would certainly be more appealing, but as mentioned in the introduction, current technology limits 3-D PIV to flow speeds many

orders of magnitude lower than what was used for this research. Modifying the pulse burst laser to perform 3-D PIV experiments could be an avenue worth exploring. In its current setup, the pulse burst laser is capable of near-MHz rate scans, so with some clever modifications it might be possible to perform experiments at flow speeds previously uncharted for 3-D PIV.

It would also be interesting to resolve structures in the inner layer and investigate the effect of these structures to the presence of large-scale structures in the outer layer. A two-point tagging technique similar to the one used by Smits and Delo (discussed in section 1.4) might be useful to resolve these structures while utilizing the 3-D flow visualization technique used in this research.

Time-resolved data would be extremely helpful in investigating the evolution of these structures, but current technological capabilities would again be a hindrance. While Smits and Delo (1997) investigated these structures using time-resolved data (40 ms between subsequent volumes), their flow speed was 229 mm/s, but the flow speed used for this thesis was over 100 times faster. That would likely mean that the time between subsequent volumes for this research would need to be 100 times faster, or 40 μs – that is 3 times faster than the volumetric scanning rate used in our experimental setup! A redesign of the experimental setup could facilitate time resolution at the expense of spatial resolution. Specifically, it might be possible to use 20 pulses instead of 68 in order to produce faster volumetric scans, but it would likely be necessary to reduce the scanning distance in order to maintain strong spatial resolution. Alternatively, the development of a faster scanning mirror would solve this problem. On top of all of these considerations, a more capable camera would have to be used in order to store a sufficient

amount of images over a small time frame. The Ultra68 camera used currently can only store 68 images at a time, making it a severely limiting tool for time resolution. More capable cameras are available but are extremely expensive, making their purchase nontrivial. Disregarding time resolution, a more advanced camera would be beneficial even for experiments of the kind presented in this thesis.

It is reassuring to know that there are many improvements that could be made to the turbulent boundary layer facility, with many of them being technological. As advancements are made, stronger measurements can be taken and more conclusions can be drawn about this flow field. The preliminary nature of the experiments presented in this thesis displayed the capabilities of the current visualization techniques used, and the results from these novel techniques were strong. The fact that these results could be improved upon using new technologies innovatively as they become available is quite exciting.

6 CONCLUSIONS

The use of 2-D PIV and 3-D flow visualization to analyze coherent structures in a turbulent boundary layer with a freestream flow velocity of 100 feet per second was demonstrated. The experimental setup was tested by pitot probe measurements and PIV data to confirm that the flow seeding for the 3-D experiments was constrained to the boundary layer and that a nominally-zero pressure gradient turbulent boundary layer was being produced.

The most difficult part of the research was implementing a satisfactory flow seeding technique for both PIV and 3-D flow visualization. For the PIV measurements, the best flow seeding technique involved seeding the entire room with smoke particles and allowing the open-circuit wind tunnel to continually recirculate the particles. Care had to be taken to provide enough particles for the PIV software to be able to resolve the flow field while not providing so many particles that the image pairs became noisy. After attempts at many different seeding techniques for 3-D flow visualization, it was decided that the best technique would incorporate ideas from previous literature where a slit was cut on the flat plate to introduce smoke particles into the boundary layer. The flow seeding technique for 3-D experiments proved satisfactory and revealed some interesting structures while maintaining strong resolution. The PIV data gave strong quantitative data as revealed by the momentum contour plots, but would be even more effective if the data could be directly correlated with the qualitative 3-D measurements. Both of these techniques should provide a strong platform for future measurements involving a

multitude of flow conditions such as adverse pressure gradients, and with some modification to the experimental arrangement, simultaneous PIV and 3-D flow visualization should be possible. Hence, the next step for the development of this measurement technique would be to investigate the effectiveness of simultaneous PIV and 3-D flow visualization measurements in quantifying the large-scale structures in the outer region of the boundary layer. This will be especially helpful because it will allow direct comparisons of the Reynolds stresses, vorticity, and other statistical quantities that result from the presence of these structures. It would not come without difficulty though, and would require more experimentation with flow seeding techniques as the boundary layer would need to be strongly seeded in comparison to the freestream flow, but not seeded so strongly as to make PIV measurements impossible in the boundary layer. This will be a very interesting challenge to tackle, but the results from this technique will be worthwhile since 3-D PIV experiments are not currently possible for flow speeds of this magnitude. Changes in flow conditions, namely the presence of varying pressure gradients and flow control devices, would provide direct comparisons between the resulting data from these flow conditions and the data acquired in this thesis. Changes in the shapes and sizes of the structures in the boundary layer could be observed and comments could be made regarding the effect of these flow conditions on the boundary layer, particularly if supplemented by 2-D PIV data.

REFERENCES

[1] Pope, Stephen B., "Ten questions concerning the large-eddy simulation of turbulent flows," New Journal of Physics, Vol 6, No 3, 2004.

[2] Adrian, R. J., "Scattering particle characteristics and their effect on pulsed laser measurements of fluid flow: speckle velocimetry vs particle image velocimetry," Applied Optics, Vol 23, pp. 1690-91, 1984.

[3] Adrian, R.J., "Twenty years of particle image velocimetry". Experiments in Fluids, Vol 39, pp. 159–169, 2005.

[4] Maas, H., Putze, T., and Westfield, P., "Recent Developments in 3D-PTV and Tomo-PIV," Notes on Numerical Fluid Mechanics and Multidisciplinary Design, Vol. 106, pp. 53-62, 2009.

[5] Barreras, F., Lozano, A., Yates, A. J., and Dopazo, C., "The structure of subsonic air wakes behind a flat plate," Experiments in Fluids, Vol. 26, pp. 478-480, 1999.

[6] Pope, Stephen B., *Turbulent Flows*, 1st edition, Cambridge University Press, New York, 2000, Chap 6.

[7] Davidson, P. A., *Turbulence: an Introduction for Scientists and Engineers*, 1st edition, Oxford Press, New York, 2004, Chaps. 3, 4.

[8] Head, M. R., and Bandyopadhyay, P., "New Aspects of Turbulent Boundary-Layer Structure," Journal of Fluid Mechanics, Vol. 107, pp. 297-338, 1981

[9] Falco, R. E., "Coherent motions in the outer region of turbulent boundary layers," The Physics of Fluids, Vol. 20, pp. 124-132, October 1977.

[10] Jansen, Bernard J., "Flow Visualization Through the Use of the Smoke Wire Technique," AIAA paper 81-0412, 1981.

[11] Worth, N. A., and Nickels, T. B., "An Experimental Demonstration of Accelerated Tomo-PIV," Springer Proceedings in Physics, Vol. 131, pp 57-60, 2009.

[12] Delo, C. and Smits, A. J., "Volumetric Visualization of Coherent Structure in a Low Reynolds Number Turbulent Boundary Layer," International Journal of Fluid Dynamics, Vol. 1, Article 3, 1997.

[13] Adrian, R. J., Meinhart, C. D., and Tomkins, C. D., "Vortex organization in the outer region of the turbulent boundary layer," Journal of Fluid Mechanics, Vol. 422, pp. 1-54, November 2000.

[14] Raffel, M., Willert, C., and Kompenhans, J., *Particle Image Velocimetry: a Practical Guide*, 1st edition, Springer, Germany, 1998, Chaps 1-3, 5.

[15] Lynch, K., and Thurow, B., "Three dimensional flow visualization using a pulse burst laser system," AIAA Region II Student Conference, Cocoa Beach, FL, March 2008.

[16] Thurow, B. and Satija, A., "Design of a MHz Repetition Rate Pulse Burst Laser System at Auburn University," AIAA Paper 2006-1384, 44th AIAA Aerospace Sciences Meeting, Reno, NV, 2006.

[17] Thurow, B., Satija, A., and Lynch, K., "3rd generation MHz rate pulse burst laser system," Applied Optics, Vol. 48, Issue 11, pp. 2086-2093, 2009.

[18] Lynch, Kyle P. and Thurow, Brian S., "Investigation of Image Processing Steps for Reconstruction of Three-Dimensional Flow Visualization Images," AIAA paper 2008-4269, 2008.

[19] Roach, P.E., Brierley, D.H., "The Influence of a Turbulent Free-Stream on Zero Pressure Gradient Transitional Boundary Layer Development. Part 1: Test Cases T3A and T3B," ERCOFTAC Workshop, Lausanne, 1990.

[20] Shetz, J., *Boundary Layer Analysis*, 1st edition, Prentice Hall, Upper Saddle River, New Jersey, 1992.

[21] De Chant, L. A., "The venerable 1/7th power law turbulent velocity profile: a classical nonlinear boundary value problem solution and its relationship to stochastic processes," Applied Mathematics and Computation, Vol. 161, Issue 2, pp. 463-474, 2005.

[22] "Fang, F. and Farell, C., "Turbulent boundary layer characteristics along the centerline of a contracting wall," Journal of Wind Engineering and Industrial Aerodynamics, Vol 61, Issues 2-3, pp. 131-151, 1996.

[23] Kendall, A. and Koochesfahani, M., "A method for estimating wall friction in turbulent wall-bounded flows,' Exp Fluids paper 44:773–780, 2008.

[24] Spalding, D. B., "A single formula for the Law of the Wall," J Appl Mech, Trans ASME Ser E. 83:455, 1961.

[25] Klebanoff, P. S., "Characteristics of Turbulence in a Boundary Layer with Zero Pressure Gradient," NACA report 1247, 1955.

[26] DeGraaff, D. B. and Eaton, J. K., "Reynolds Number Scaling of the Flat Plate Turbulent Boundary Layer," J Fluid Mech, Vol 422, pp. 319-346.

APPENDIX A – MATLAB CODE FOR PIV

The following is a MATLAB code for analyzing the PIV data processed by PIVPROC. This code utilizes a function called "piv_vec2mtx" written by Kyle Lynch in the Auburn University Advanced Laser Diagnostics Laboratory that takes the .VEC file output by PIVPROC and converts it into an m x n x 2 matrix, where m and n are the x and y interrogation regions, respectively, m x n x 1 is the u-component of velocity and m x n x 2 is the v-component of velocity.

```
% vector averaging file

clear all
clc

ppi = 480; %pixels per inch
dt = 0.000015; %delta t (seconds)
AR = 1; %aspect ratio used in PIVPROC iterations
freestream = 100; %maximum velocity shown in the PIV measurements

n=165; %total number of vector files

dirfile='F:\Tyler\Research\PIV data\good100';
dirsave='F:\Tyler\Research\PIV data\good100';

% vectors_avg=zeros(128,84,2,165*4);
```

```matlab
for folder=1:4


    for sequence=1:n
        if sequence<10
            filename  =  fullfile(dirfile,[num2str(folder)],[num2str(folder)  '_000' num2str(sequence) '.VEC']);
%original file directory
            savefile = fullfile(dirsave,[num2str(folder) '_000' num2str(sequence)]);

            savefile2 = fullfile(dirsave,[num2str(folder) '_000' num2str(sequence) 'momentum']);
        elseif sequence<100
            filename  =  fullfile(dirfile,[num2str(folder)],[num2str(folder)  '_00'  num2str(sequence)  '.VEC']);
%original file directory
            savefile = fullfile(dirsave,[num2str(folder) '_00' num2str(sequence)]);

            savefile2 = fullfile(dirsave,[num2str(folder) '_00' num2str(sequence) 'momentum']);
        elseif sequence<1000
            filename  =  fullfile(dirfile,[num2str(folder)],[num2str(folder)  '_0'  num2str(sequence)  '.VEC']);
%original file directory
            savefile = fullfile(dirsave,[num2str(folder) '_0' num2str(sequence)]);

            savefile2 = fullfile(dirsave,[num2str(folder) '_0' num2str(sequence) 'momentum']);
        end
%     vectors_avg(:,:,:,sequence+(n*(folder-1)))=piv_vec2mtx(filename,ppi,dt);
        vectors=piv_vec2mtx(filename,ppi,dt);


%     save(savefile,'vectors')


        individual(vectors,filename,savefile,savefile2,ppi,dt,AR,freestream);
%for individual files
```

```
    end

end


save('vectors_avg')


% average(vectors_avg,filename,ppi,dt,AR,freestream,n);


function individual(vectors,filename,savefile,savefile2,ppi,dt,AR,freestream)
%This function takes the individual runs and produces spanwise vorticity,
%quiver, and momentum contour plots that are saved in a folder specified by
%the user in the "savefile", "savefile2", and "savefile3" variables. It
%also saves an Excel spreadsheet compatible with Tecplot in the folder
%specified by the "savefile" variable.


% [omega,angularvelocity] = curl(vectors(:,:,1),vectors(:,:,2));
%
% range=[-1 5];
%
% I3=figure(3);
% contour(flipdim(angularvelocity,1),range)
% colorbar
% axis([0 84 0 125])
% set(gca,'XTick',0:(84/2):84)
% set(gca, 'XTickLabel',[0:1.3:2.6]);
% set(gca,'YTick',0:(125/2):125)
% set(gca,'YTickLabel',[0:1:1.8]);
% xlabel('x (in)')
% ylabel('y (in)')
```

```
% saveas(I3,savefile,'bmp')

% saveas(I3,savefile,'fig')

% close(3)


vectors(:,:,1)=vectors(:,:,1)+0.8*freestream;


%Figure 1 is the quiver plot. Figure 2 is the momentum layer plot.


I=figure(1);

quiver(flipdim(vectors(:,:,1),1),flipdim(vectors(:,:,2),1),3,'.k')

axis([0 82 0 61])

set(gca,'XTick',0:(82/2):82)

set(gca, 'XTickLabel',[0:1.3:2.6]);

set(gca,'YTick',0:(61/2):61)

set(gca,'YTickLabel',[0:1:2]);

xlabel('x (in)')

ylabel('y (in)')

saveas(I,savefile,'bmp')

saveas(I,savefile,'fig')

close(1)


I2=figure(2);

contourf(flipdim(vectors(:,:,1),1),5)

colormap(gray)

axis([0 82 0 61])

set(gca,'XTick',0:(82/2):82)

set(gca, 'XTickLabel',[0:1.3:2.6]);

set(gca,'YTick',0:(61/2):61)
```

```
set(gca,'YTickLabel',[0:1:2]);

xlabel('x (in)')

ylabel('y (in)')

saveas(I2,savefile2,'bmp')

saveas(I2,savefile2,'fig')

close(2)


vectordim = size(vectors);

b=1;

for n=1:(vectordim(1)) %n corresponds to x position

    for m=1:(vectordim(2)) %m corresponds to y position

        u(b)=1.5*vectors(n,m,1);

        v(b)=vectors(n,m,2);

        x(b)=2.6/84*m; %FOV was 2.6 inches in x-direction

        y(b)=2/62*(62-n); %FOC was 2 inches in y-direction

        b=b+1;

    end

end


vectordim2 = size(u);

xyuv = zeros(vectordim2(2),7);

xyuv(:,1) = x';

xyuv(:,2) = y';

xyuv(:,3) = u';

xyuv(:,4) = v';


uprime = xyuv(:,3)+0.8*freestream; %adding because vectors are negative
```

```
xyuv(:,5) = uprime;

xlswrite(savefile,xyuv)

end

function average(vectors_avg,filename,ppi,dt,AR,freestream,n)

%This portion of the code takes information from every vector file and
%averages the values. They are then placed into an Excel spreadsheet
%compatible with Tecplot.

vectorsum=zeros(61,82,2);

n=4*165;

for sequence=1:n
    vectorsum=vectorsum+vectors_avg(:,:,:,sequence);
end

vector_avg=vectorsum/sequence;

save vector_avg

vectordim = size(vector_avg);
b=1;
for n=1:(vectordim(1)) %n corresponds to x position
    for m=1:(vectordim(2)) %m corresponds to y position
```

```matlab
%        u(b)=vectors_avg(n,m,1)*1/ppi*(1/12)*(1/dt);

%        v(b)=vectors_avg(n,m,2)*1/ppi*(1/12)*(1/dt);

        u(b)=vector_avg(n,m,1);

        v(b)=vector_avg(n,m,2);

        x(b)=2.6/82*m; %FOV was 2.6 inches in x-direction

        y(b)=2/61*(61-n); %FOC was 2 inches in y-direction

        b=b+1;

    end

end


vectordim2 = size(u);

xyuv = zeros(vectordim2(2),4);

xyuv(:,1) = x';

xyuv(:,2) = y';

xyuv(:,3) = u';

xyuv(:,4) = v';


% filename='100_5ft_smallparticles';

% xlswrite(filename,xyuv)


figure(1)

contourf(flipdim(vector_avg(:,:,1),1),20)

axis([0 82 0 61])

set(gca,'XTick',0:(82/2):82)

set(gca, 'XTickLabel',[0:1.3:2.6]);

set(gca,'YTick',0:(61/2):61)

set(gca,'YTickLabel',[0:1:2]);

xlabel('x (in)')
```

```
ylabel('y (in)')


end
```

APPENDIX B – MATLAB CODE FOR BOUNDARY LAYER PROFILE

This is a MATLAB code for calculating the boundary layer profile from the resulting averaged values from PIV and pitot probe measurements. The code reads the values from an existing Microsoft Excel spreadsheet where the user can find 99% of the freestream value to find the boundary layer thickness in the PIV data. The user then inputs the range of values that corresponds to the boundary layer into MATLAB as well as the boundary layer thickness, and the boundary layer profile is plotted. The pitot probe profile is averaged separately and put into its own Excel spreadsheet for loading by MATLAB.

```
%Boundary Layer Profile


clc
clear all


%Read XLS files.  Variables are n x 5 where the columns are x, y, u, v, and
%u' respectively.
pitot=xlsread('G:\MATLAB Code\pitot.xls');
piv=xlsread('G:\MATLAB Code\100_5ft.xls');


u=piv(5751:5875,3);


%Find freestream and use to find delta manually in Excel
```

```matlab
freestream=min(piv(5751:5875,3)) %corresponds to delta = 1.21 in


% Find delta

delta=1.21;


%Create profile for PIV

yoverdelta=piv(5799:5875,2)/delta;

uoverue=piv(5799:5875,3)/(0.99*freestream);


%Create profile for pitot

uoveruepitot=pitot(:,1);

yoverdeltapitot=pitot(:,2); %delta measured to be 1.21 in


%1/7th power law profile

for k=1:125

    yoverdelta2(k)=k/125;

    uoverue2(k)=yoverdelta2(k)^(1/7);

end


figure(1)

plot(uoverue,yoverdelta,'-.k',uoveruepitot,yoverdeltapitot,':k',uoverue2,yoverdelta2,'--k')

legend('PIV','Pitot','1/7th power law')

xlabel('u/U')

ylabel('y/delta')

axis([0 1 0 1])
```

APPENDIX C – MATLAB CODE FOR 3-D IMAGE POST-PROCESSING

The following is a MATLAB code giving an example of the post-processing techniques applied to the 3-D image sequences. The code includes conversion to a .mat file, thresholding, column normalization, and the application of a smoothing filter, all of which are discussed in section 3. The code will then process figures of the 34th image after each correction is implemented for comparisons. A 3-D isosurface plot is also included for a 3-D visualization of the image.

```
clc
clear all

dir_source='E:\3-D BL 030110\Sequences\'
dir_save='F:\Tyler\MATLAB image files\'

nframes=68;
sequence=1;

for frame = 1:nframes
   if (frame - 1) < 10
      filestring = fullfile(dir_source,['Sequence' num2str(sequence) '_00' num2str(frame-1) '.tif']);
   else
      filestring = fullfile(dir_source,['Sequence' num2str(sequence) '_0' num2str(frame-1) '.tif']);
   end
   image(:,:,frame) = double(imread(filestring,'PixelRegion',{[1 220],[2 220]}));
```

```matlab
end


for n=34
    figure(1)
    imagesc(image(:,:,n))
    title('Original image')
    colorbar
    colormap(gray)
    title(n)
end


threshold=100;


image(image<threshold)=0;


for n=34
    figure(2)
    imagesc(image(:,:,n))
    colorbar
    title('After thresholding')
    colormap(gray)
end


for n=1:nframes

    i=1;

    for b=181:220
```

```
        norm(i,:)=image(b,:,n);

        i=i+1;

    end


    norm=sum(norm(:,:))/(i-1);


    for col=1:219

        image(:,col,n)=image(:,col,n)/norm(1,col);

    end


end


for n=34

    figure(3)

    imagesc(image(:,:,n))

    colorbar

    title('After thresholding and normalization')

    colormap(gray)

end


image(:,:,:)=smooth3(image(:,:,:),'box',[3 3 3]);


for n=34

    figure(4)

    imagesc(image(:,:,n))

    colorbar

    title('After thresholding, normalization, and filtering')

    colormap(gray)
```

```
end
```

```
figure(5)
```

```
isosurface(image,0.3)
```

APPENDIX D – 3-D FLOW VISUALIZATION IMAGES

3-D flow visualization images that were not presented in section 5 are presented here for the reader to see more examples of the images to become more familiarized with the flow field.

99

101

103